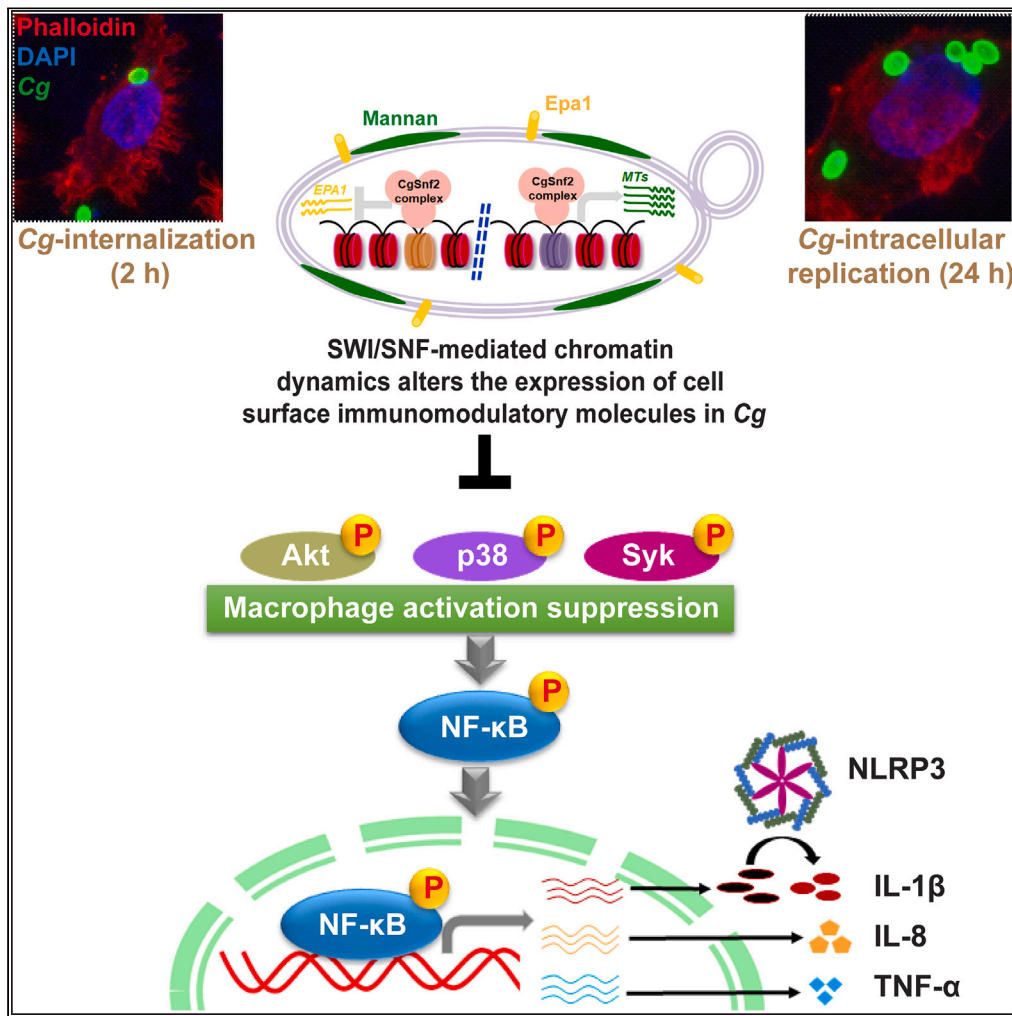**Article**

SWI/SNF complex-mediated chromatin remodeling in *Candida glabrata* promotes immune evasion

Kundan Kumar,
Aditi Pareek,
Rupinder Kaur

rkaur@cdfd.org.in

Highlights

Macrophage-internalized *Candida glabrata* contains 12,000 dynamic nucleosomes

CgSnf2 is pivotal to the macrophage milieu-induced transcriptional reprogramming

SWI/SNF complex governs the nucleosome occupancy and expression of the *EPA1* adhesin gene

Epa1 surface exposure modulates NF-κB signaling-dependent IL-1β secretion

Article

SWI/SNF complex-mediated chromatin remodeling in *Candida glabrata* promotes immune evasion

Kundan Kumar,[1] Aditi Pareek,[1,2] and Rupinder Kaur[1,3,*]

SUMMARY

Immune evasion is critical for fungal virulence. However, how the human opportunistic pathogen *Candida glabrata* (*Cg*) accomplishes this is unknown. Here, we present the first genome-wide nucleosome map of the macrophage-internalized *Cg* consisting of ∼12,000 dynamic and 70,000 total nucleosomes. We demonstrate that CgSnf2 (SWI/SNF chromatin remodeling complex-ATPase subunit)-mediated chromatin reorganization in macrophage-internalized *Cg* upregulates and downregulates the immunosuppressive seven-gene mannosyltransferase-cluster (*CgMT-C*) and immunostimulatory cell surface adhesin-encoding *EPA1* gene, respectively. Consistently, *EPA1* overexpression and *CgMT-C* deletion elevated IL-1β (pro-inflammatory cytokine) production and diminished *Cg* proliferation in macrophages. Further, *Cgsnf2Δ* had higher Epa1 surface expression, and evoked increased IL-1β secretion, and was killed in macrophages. Akt-, p38-, NF-κB- or NLRP3 inflammasome-inhibition partially reversed increased IL-1β secretion in *Cgsnf2Δ*-infected macrophages. Importantly, macrophages responded to multiple *Candida* pathogens via NF-κB-dependent IL-1β production, underscoring NF-κB signaling's role in fungal diseases. Altogether, our findings directly link the nucleosome positioning-based chromatin remodeling to fungal immunomodulatory molecule expression.

INTRODUCTION

Fungal infections cause >1.6 million deaths annually.[1] *Candida* species are the most common cause of invasive fungal infections, with *Candida* (*Nakaseomyces*) *glabrata* being the second-to-fourth most prevalent *Candida* infectious agent, based upon the geographical location.[1–5] *C. glabrata* (*Cg*) invasive infections are associated with mortality rate exceeding 35%.[6–8] *Cg* has recently been classified as a fungal pathogen of high-priority by the World Health Organization.[9]

Cg is evolutionarily closer to the budding yeast *Saccharomyces cerevisiae*.[4,5] It lacks secreted proteolytic activity and hyphal formation, and predominantly banks upon the stealth strategy to persist in the host.[4,10,11] *Cg* circumvents the host immune system by inhibiting phagolysosome acidification and restricting pro-inflammatory cytokine IL-1β production in macrophages.[4] Further, the type I interferon signaling contributes to *Cg* immune evasion by dysregulating iron and zinc homeostasis in macrophages.[12,13]

Cg infection to macrophages induces transcriptomic changes in both macrophages and macrophage-internalized *Cg*, with *Cg* relying on multiple mechanisms including chromatin heterochromatinization, carbon metabolism reprogramming, autophagy induction, and cell surface reconfiguration to thwart macrophage anti-*Cg* response, and proliferate in macrophages.[4,10,11,14–17] Notably, *Cg* invokes low levels of IL-1β production in macrophages, and during vaginal and systemic infections.[17–19] Macrophages activate NLRP3 inflammasome and produce IL-1β in a spleen tyrosine kinase (Syk) signalling-dependent manner, in response to *Cg* infection.[17] *Cg* restricts IL-1β secretion in infected-macrophages via a family of eleven putative glycosylphosphatidylinositol (GPI)-linked cell surface-associated proteases (CgYps1-11; CgYapsins).[17] Consistently, *CgYPS1-11* loss led to increased IL-1β secretion and *Cg* killing in macrophages, and *Cg* clearance from mice organs.[14,17]

Another important intracellular survival strategy of *Cg* involves chromatin reconfiguration, with CgRtt109 (Histone H3 lysine-56 acetyltransferase) and two subunits of RSC chromatin remodeling complex (CRC), CgRsc3A and CgRsc3B, being required for *Cg* proliferation in macrophages.[20] Macrophage-internalized *Cg* displayed elevated lysine deacetylase activity, and an increase and a decrease in closed and open-chromatin marks, respectively, with remodelled-chromatin linking metabolic adaptation and energy homeostasis to *Cg* replication.[20] Further, 6 h and 10 h of macrophage internalization rendered *Cg* chromatin resistant to micrococcal nuclease (MNase) digestion, indicating a widespread chromatin reorganization.[20] A nucleosome, consisting of 147 bp DNA wrapped around the histone octamer, is the fundamental repeating subunit of chromatin, and nucleosome dynamics governs chromatin structure and functions.[21] Nucleosomes occupy defined positions in the genome, with DNA sequence, CRCs, transcriptional regulators and RNA polymerase II (RNAPII) transcription machinery acting in conjunction to maintain nucleosome locations.[21] Nucleosome positioning control DNA accessibility to various enzymes and regulatory

[1]Laboratory of Fungal Pathogenesis, Centre for DNA Fingerprinting and Diagnostics, Hyderabad 500039, India
[2]Graduate studies, Manipal Academy of Higher Education, Manipal, Karnataka 576104, India
[3]Lead contact
*Correspondence: rkaur@cdfd.org.in
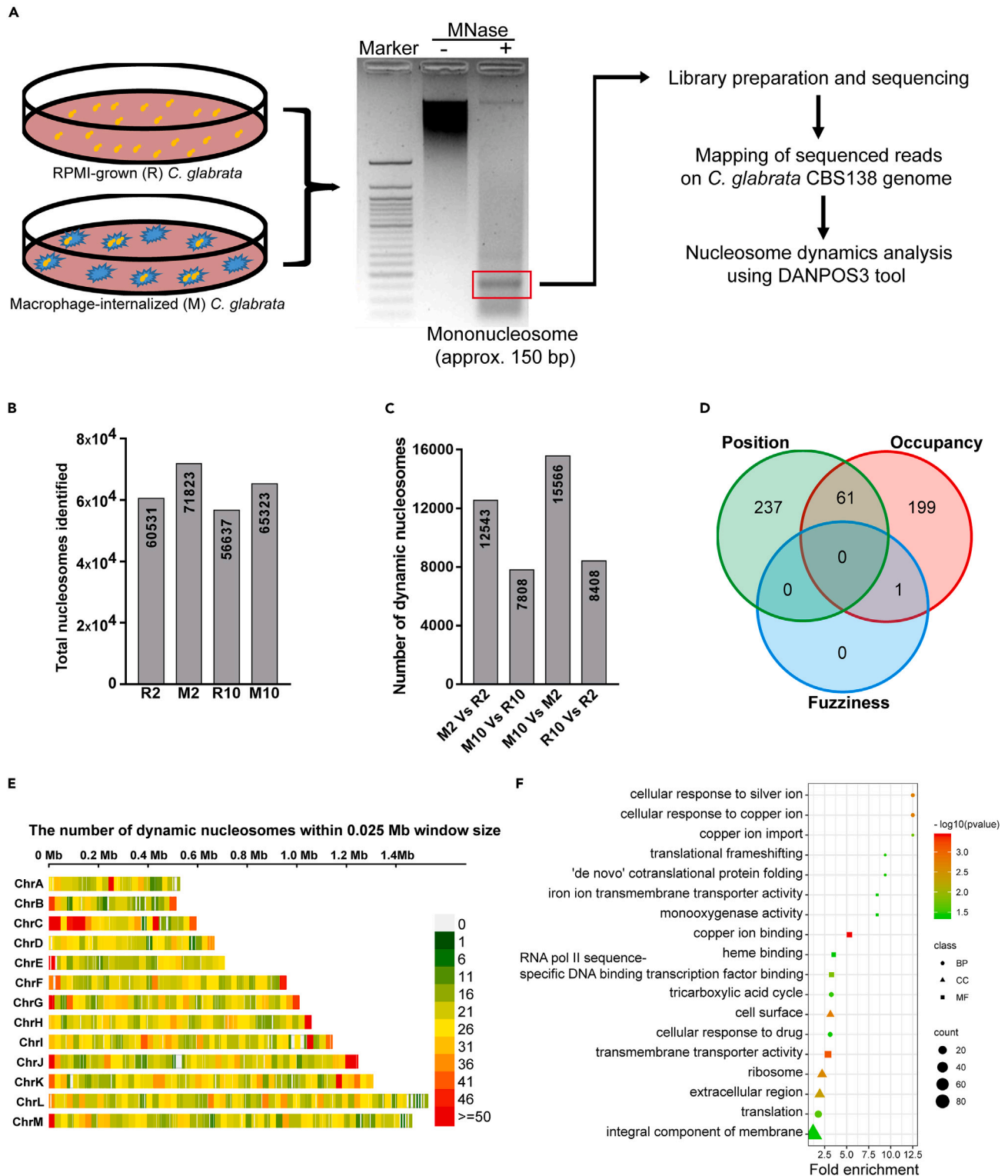https://doi.org/10.1016/j.isci.2024.109607

Figure 1. Genome-wide nucleosome dynamics in response to the macrophage milieu

(A) Experimental design diagram for nucleosome mapping in *Cg wild-type* cells that were grown either in RPMI medium or infected to THP-1 macrophages for 2 h and 10 h.

(B) Total nucleosomes identified using the dpos function of DANPOS3 tool with default parameters. R2: 2 h RPMI-grown, R10: 10 h RPMI-grown, M2: 2 h macrophage-internalized and M10: 10 h macrophage-internalized *Cg* cells.

Figure 1. *Continued*

(C) Dynamic nucleosomes identified in indicated compared datasets.

(D) Venn diagram showing the overlap in the number of genes that exhibited position shift, occupancy, and fuzziness changes at their promoter regions in M2 versus R2 comparison.

(E) Chromosome-wise distribution of dynamic nucleosomes in M2 versus R2 comparison. The color scale indicates nucleosome density.

(F) Gene Ontology (GO) terms for biological process (BP), cellular component (CC) and molecular function (MF) enriched in genes with dynamic nucleosomes at their promoters in M2 versus R2 comparison.

See also Figures S1 and S2; Tables S1–S3.

proteins.[21,22] The nucleosome-depleted regions (NDRs), and/or chromatin regions opened up locally by CRCs, facilitate the binding of transcription factors and RNAPII machinery to DNA, thereby promoting gene expression.[21,22]

ATP-dependent CRCs mobilize nucleosomes via DNA translocation, histone exchange and/or DNA-histone disengagement.[22] These belong to four subfamilies: imitation switch (ISWI), chromodomain helicase DNA-binding (CHD), SWI/SNF (SWItch/Sucrose Non-Fermentable), and INO80 (INOsitol requiring), with their catalytic ATPase subunit aiding in DNA translocation.[22] The SWI/SNF complex in *Cg* and *S. cerevisiae* consists of 12 subunits.[23] Transcription factors recruit the SWI/SNF complex at specific DNA sites in *S. cerevisiae*, with ScSnf2 involved in DNA binding.[22] Notably, ScSnf2 localizes to NDRs, and controls transcription initiation by governing +1 nucleosome (transcription start site-associated) position.[24]

Despite chromatin architecture being pivotal to the intracellular survival of *Cg*, the nucleosome landscape of macrophage-internalized *Cg* is undefined. Here, we report the first genome-wide nucleosome map of macrophage-internalized *Cg* consisting of ~70,000 nucleosomes, including 12,000 nucleosomes that exhibited changes in position, occupancy, or fuzziness. Additionally, we present the roles of seven ATP-dependent CRCs in *Cg* pathobiology, underscoring the essentiality of CgSnf2 for immune evasion and virulence. Altogether, our findings unify two central virulence mechanisms, viz., chromatin restructuring and immune evasion, in *Cg*.

RESULTS

Micrococcal nuclease-Sequencing analysis reveals nucleosome dynamics in macrophage-internalized *C. glabrata*

Nucleosome dynamics encompasses nucleosome position shifts, occupancy changes, and fuzziness changes, which represent changes in nucleosome genomic location, local density, and deviation from the most preferred position for each unit in a cell population, respectively.[21,22,25] To investigate nucleosome dynamics, we performed MNase-Seq analysis in 2 h and 10 h macrophage-internalized and RPMI-grown *Cg* cells (Figure 1A). We identified 56,637-71,823 nucleosomes under four-studied conditions (Figure 1B; Table S1), with 12–24% exhibiting changes in position, occupancy, or fuzziness (Figures 1C and 1D; Table S2). Most nucleosomes displayed a fuzziness score of 50–60 (Figure S1A). Most of the chromosome contained a high number of dynamic nucleosomes at their ends (Figure 1E). Further, gene bodies displayed the largest number of nucleosomes (Figures S1B and S1C). Compared to RPMI-grown cells, 5–6% more dynamic nucleosomes were mapped to intergenic regions in macrophage-internalized *Cg* (Figure S1D). Notably, 5% of dynamic nucleosomes were present in promoter regions across the four compared datasets (Figure S1E), and nucleosome fuzziness was the least observed change in all comparisons (Figures 1D, S2A–S2C; Table S2).

Consistent with the macrophage-induced largescale chromatin changes,[20] nucleosomes in 10 h macrophage-internalized *Cg* were more dynamic, compared to 2 h macrophage-internalized *Cg* (Figure 1C), with position shift being the predominant change (Figure S2B). 10 h macrophage-internalization also led to the highest gain in the nucleosome occupancy (Figure S1F) and the lowest dynamic nucleosome numbers at the gene promoters (Figure S1E; Table S3), compared to the growth in RPMI medium, which is consistent with the genome heterochromatinization of the mid-phase macrophage-internalized *Cg*.[20]

DAVID functional enrichment analysis[26,27] revealed that promoters of the genes, belonging to the GO (Gene Ontology) terms, cell surface, translation, copper ion import, and tricarboxylic acid (TCA) cycle, displayed altered nucleosome configurations in 2 h macrophage-internalized *Cg*, with translation gene promoters showing high nucleosome occupancy (Figure 1F; Table S3). Notably, TCA cycle and translation genes in *Cg* are known to be upregulated and downregulated, respectively, in response to the macrophage milieu.[14,20] Further, compared to 2 h, 10 h macrophage internalization led to dynamic nucleosomes in promoters of the genes that belonged to GO terms, fungal-type cell wall, translation and adhesion of symbiont to host (Figure S2D; Table S3). Notably, fungal-type cell wall gene promoters contained dynamic nucleosomes in both 10 h macrophage-internalized and 10 h RPMI-grown *Cg*, compared to 10 h and 2 h RPMI-grown *Cg*, respectively (Figures S2E and S2F; Table S3), indicating the contribution of chromatin changes to the cell wall gene expression plasticity under both RPMI-growth and macrophage-internalization conditions.

We draw six major conclusions from our MNase-Seq data which report nucleosome dynamics for the first time in a host cell-internalized eukaryotic pathogen. First, promoter regions in *Cg* are nucleosome-depleted, consistent with a previous study.[28] Second, 10–20% nucleosomes displayed changes in position, occupancy, or fuzziness upon macrophage internalization. Third, the macrophage-induced transcriptional downregulation and upregulation, respectively, of translation and TCA cycle genes may be governed by increased and decreased nucleosome occupancy at the respective gene promoters. Fourth, nucleosome positioning is likely to be a key determinant of cell wall gene expression levels. Fifth, compared to gene bodies, dynamic nucleosomes were double in number at the promoter and intergenic regions after 2 h macrophage internalization, with genes containing these dynamic nucleosomes potentially involved in copper and iron transport, TCA cycle, translation, and cellular signaling (Figure 1F). Finally, position shift was the most common nucleosome dynamic event in *Cg*. Altogether, besides unveiling the macrophage milieu-induced gene-specific nucleosome pattern in *Cg*, our findings raise the possibility that CRCs, which are essential for nucleosome dynamics, may drive *Cg* survival in macrophages.

Chromatin remodeling complexes modulate intracellular survival of *C. glabrata*

Cg possesses seven ATP-dependent CRCs. To elucidate their functions, we generated six deletion strains, *Cgsnf2Δ*, *Cgisw1Δ*, *Cgisw2Δ*, *Cgchd1Δ*, *Cgino80Δ*, and *Cgswr1Δ*, for non-essential genes that encode putative ATPase subunits of SWI/SNF, ISWI, ISWI, CHD1, INO80 and INO80 CRC subfamilies, respectively (Figure S3A). Despite multiple attempts, *CgSTH1* (encodes RSC complex ATPase) could not be deleted, which may reflect CgSth1 essentiality for growth. Next, we examined stress susceptibility and virulence-associated traits in generated mutants. Since *Cgrsc3aΔbΔ* was previously reported to display reduced survival in macrophages and mice,[20] we included this mutant in our analysis as well. Phenotypic profiling revealed pleiotropic stress, and low pH and high iron sensitivity of *Cgsnf2Δ* and *Cgswr1Δ* mutants, respectively, (Figure 2A). *Cgsnf2Δ* also exhibited elongated cell morphology (Figure S3B), and grew slowly in both YPD and RPMI medium at 37°C (Figure S3C). These results indicate a central role for CgSnf2 in cell growth and stress survival. Notably, *Cgrsc3aΔbΔ* and *Cgino80Δ* could not utilize the alternate carbon sources and displayed reduced growth in the iron-surplus medium, with *Cgino80Δ* also showing elevated thermal stress susceptibility (Figure 2A). Further, the high-iron sensitivity of *Cgsnf2Δ*, *Cgrsc3aΔbΔ*, *Cgino80Δ*, and *Cgswr1Δ* mutants could stem from increased intracellular iron levels, due to deregulated expression of the high-affinity iron uptake, iron storage or intra-organellar iron mobilization system genes, in these mutants.

These distinct stress sensitivity phenotypes notwithstanding, three mutants, *Cgsnf2Δ*, *Cgino80Δ*, and *Cgswr1Δ*, were attenuated in their ability to form biofilms on polystyrene surface (Figure 2B). The deficient biofilm formation in *Cgsnf2Δ*, *Cgino80Δ*, and *Cgswr1Δ* mutants suggests that CgSnf2, CgIno80 and CgSwr1 chromatin remodellers are likely to regulate the expression of genes that are required for biofilm formation on inanimate surfaces such as polystyrene. Further, human THP-1 macrophage-infection analysis revealed differential survival of chromatin remodeller-mutants, with *Cgrsc3aΔbΔ* showing reduced intracellular proliferation, consistent with our previous study.[20] *Cgisw1Δ*, *Cgisw2Δ*, *Cgchd1Δ*, and *Cgswr1Δ* replicated like *wild-type* (*wt*) in THP-1 cells, while *Cgino80Δ* was defective in intracellular proliferation (Figure 2C). Contrarily, *Cgsnf2Δ* was killed in macrophages (Figure 2C), underscoring CgSnf2 essentiality for intracellular survival of *Cg*. Importantly, compared to the 500-fold increase in colony-forming units (CFUs) of *wt*, *Cgsnf2Δ* and *Cgino80Δ* CFUs were increased by 30- and 60-fold, respectively, in the RPMI medium over a period of 12 h (Figure S3D). These data suggest that *Cgsnf2Δ* killing in macrophages may not solely be due to retarded growth under tissue culture conditions. Further, CgSnf2 was crucial for *Cg* persistence in all three target organs, kidneys, liver, and spleen, in the mouse model of disseminated candidiasis, as a 5- to 100-fold lower organ fungal load was observed in *Cgsnf2Δ*-infected mice compared to *wt*-infected mice (Figure 2D). Notably, *Cgisw2Δ*- and *Cgino80Δ*-infected mice displayed 20-fold lower and 7-fold higher renal fungal burden, respectively (Figure 2D), indicating a positive and a negative role for CgIsw2 and CgIno80 in governing *Cg* fungal load in kidneys, respectively. Altogether, besides implicating ATP-dependent CRCs in diverse stress survival *in vitro*, these data underscore that while CgChd1 and CgIsw1 are dispensable for the examined pathogenesis-associated traits, CgSnf2 is required for *Cg* virulence. Notably, CgSnf2 loss has previously been associated with impaired growth and biofilm formation.[29]

CgSnf2 restrains macrophage activation

Among CRC mutants, *Cgsnf2Δ* was most severely compromised for pathogenicity, we, therefore, decided to characterize this mutant further. First, we showed through complementation analysis that the diverse stress susceptibility (Figure S4A), and the elongated cell morphology of *Cgsnf2Δ* (Figure S4B) is due to the lack of *CgSNF2*. Similarly, *CgSNF2*-expressing *Cgsnf2Δ* displayed *wt*-like survival in macrophages and mice (Figures S4C and S4D).

Since *Cg* survival in THP-1 macrophages has earlier been associated with inhibition of the NLRP3 inflammasome- and the Syk-dependent IL-1β secretion,[17] we next determined if the intracellular killing of *Cgsnf2Δ* is owing to elevated IL-1β secretion. We found 15-fold increased IL-1β secretion by *Cgsnf2Δ*-infected THP-1 macrophages, compared to *wt*-infected macrophages (Figure 3A), which was brought down by 4-fold by the NLRP3 inhibitor MCC950 (Figure 3B), with MCC950 also partially rescuing *Cgsnf2Δ*'s intracellular survival defect (Figure 3C). Notably, all other CRC mutants secreted IL-1β, similar to *wt* (Figure S4E), underscoring a unique role for CgSnf2 in *Cg*-macrophage interaction.

Next, we checked if an increased number of non-viable *Cgsnf2Δ* in THP-1 macrophages contributes to increased IL-1β levels. We found no and 3.5-fold increase in IL-1β production in heat-killed *wt*- and *Cgsnf2Δ*-infected macrophages, respectively (Figure S4F), suggesting that the intracellularly-killed *Cgsnf2Δ* are unlikely to fully account for the 15-fold elevated IL-1β secretion upon *Cgsnf2Δ* infection, and viable *Cgsnf2Δ* cells are required for macrophage activation. Notably, heat-killed *wt* evoking no IL-1β secretion in THP-1 macrophages (Figure S4F) is in accordance with the previous study.[17] Further, *Cgsnf2Δ* exhibited 2-fold higher survival in R406 (Syk inhibitor)-treated macrophages, compared to untreated macrophages (Figure 3D). *Cgsnf2Δ* was also killed in primary murine macrophages (Figure 3E), with *Cgsnf2Δ*-infected primary macrophages exhibiting 10-fold increased IL-1β levels, and MCC950 treatment diminishing the elevated IL-1β secretion (Figure 3F). These data underscore the conserved response of cultured and primary, as well as, human and mouse macrophages to *Cgsnf2Δ* infection. Collectively, these results also implicate CgSnf2 in *Cg*-mediated suppression of NLRP3 inflammasome activation, and reinforce that impeding IL-1β production is crucial for *Cg* survival in macrophages.

CgSnf2 governs transcriptional response to the macrophage internal milieu

Cg persists in macrophages in three-distinct phases, early, mid and late stage, with genome heterochromatinization being a trademark of the Mid-stage (6–12 h of macrophage-ingestion) *Cg*.[20] Notably, CRCs facilitate heterochromatin formation as well as orchestrate transcriptional regulatory proteins-target DNA interactions, that govern gene expression.[22,30] Since we could not conduct the MNase-Seq-based nucleosome profiling of macrophage-internalized *Cgsnf2Δ* due to technical limitations, we decided to profile transcriptomes of macrophage-internalized
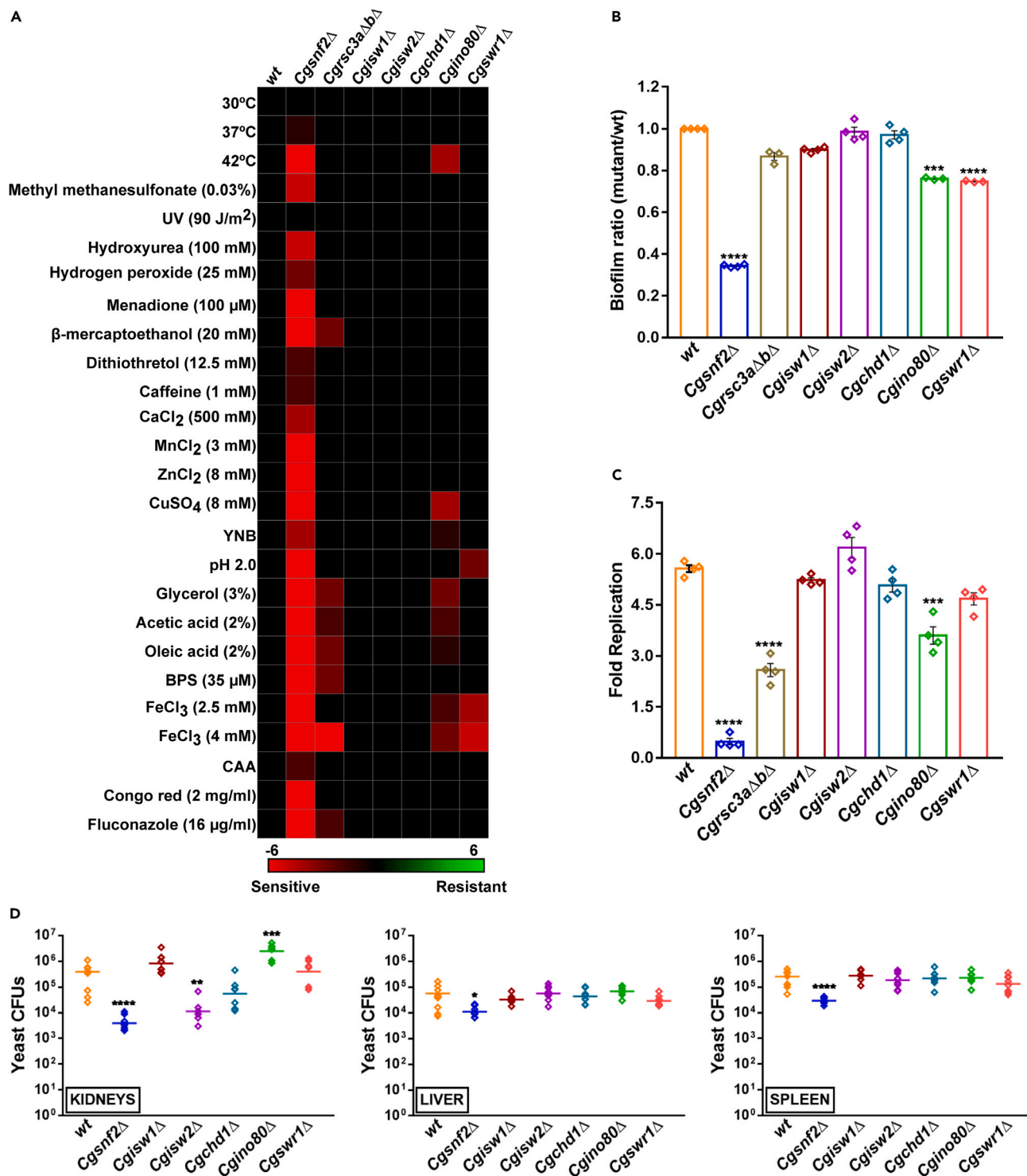
Figure 2. CgSnf2 is essential for intracellular survival and virulence

(A) Heatmap showing growth profiles of *Cg* strains. The color code depicts differences between mutant and *wt* growth under the same condition.

(B) Biofilm formation on polystyrene. Data represent mean ± SEM (n = 3–4). ***p ≤ 0.005; ****p ≤ 0.001; Paired two-tailed Student's t test.

(C) CFU-based measurement of *Cg* survival in human THP-1 macrophages. Data (mean ± SEM; n = 4) represent fold replication at 24 h. ***p ≤ 0.005; ****p ≤ 0.001; Unpaired two-tailed Student's t test.

(D) *Cg* survival in the murine model of systemic candidiasis. Diamonds and horizontal line represent fungal CFUs recovered from each mouse, and CFU geometric mean (n = 6–9) for each organ, respectively, at 7th day of infection. *p ≤ 0.05; **p ≤ 0.01; ***p ≤ 0.005; ****p ≤ 0.001; Mann-Whitney test.
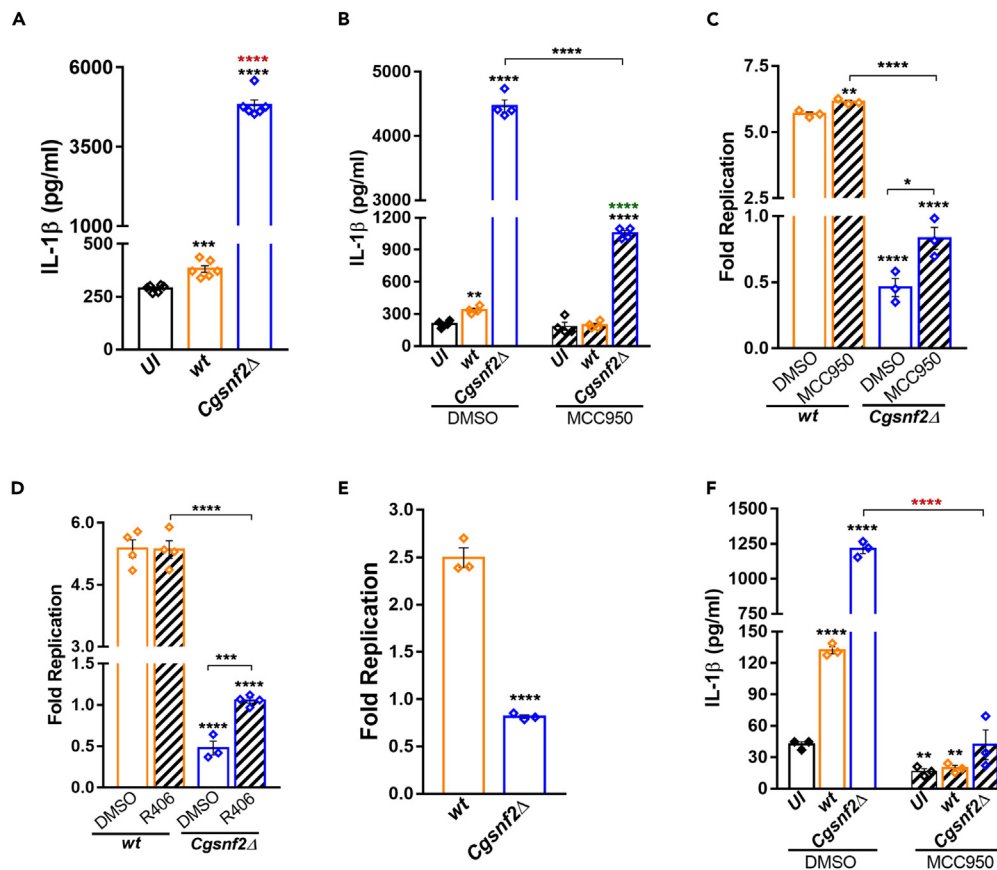
See also Figures S3 and S4.

Figure 3. CgSnf2 restrains host immune cell activation

(A) Secreted IL-1β levels by uninfected (UI) and *Cg*-infected THP-1 macrophages. Data represent mean ± SEM (n = 6). ***p ≤ 0.005; ****p ≤ 0.001; Unpaired two-tailed Student's t test. Black and red asterisks indicate statistically significant differences in IL-1β, compared to UI and *wt*-infected THP-1 cells, respectively.

(B) IL-1β secretion in uninfected or *Cg*-infected THP-1 macrophages that were treated with DMSO (solvent control) or NLRP3 inflammasome inhibitor (MCC950; 15 μM). Data represent mean ± SEM (n = 4). **p ≤ 0.01; ****p ≤ 0.001; Unpaired two-tailed Student's t test. Black and green asterisks represent statistically significant differences in IL-1β, compared to DMSO-treated uninfected and inhibitor-treated uninfected macrophages, respectively.

(C and D) *Cg* survival measurement in DMSO-, 15 μM MCC950 (C) or 5 μM R406 (Syk inhibitor) (D)-treated THP-1 macrophages. Data (mean ± SEM; n = 3–4) represent fold replication at 24 h. *p ≤ 0.05; **p ≤ 0.01; ***p ≤ 0.005; ****p ≤ 0.001; Unpaired two-tailed Student's t test.

(E) *Cg* survival measurement in murine peritoneal macrophages. Data (mean ± SEM; n = 3) represent fold replication at 24 h. ****p ≤ 0.001; Unpaired two-tailed Student's t test.

(F) IL-1β secretion in uninfected or *Cg*-infected murine peritoneal macrophages that were treated with DMSO or 15 μM MCC950. Data represent mean ± SEM (n = 3). **p ≤ 0.01; ****p ≤ 0.001; Unpaired two-tailed Student's t test. Black asterisks represent statistically significant differences in IL-1β, compared to DMSO-treated uninfected macrophages.

wt and *Cgsnf2Δ* at 2 h and 10 h post-infection via RNA-Sequencing, to uncover the molecular basis underlying CgSnf2-mediated macrophage activation abolishment. We classified genes, that showed ≥ 2-fold change in expression, as differentially expressed genes (DEGs). A total of 1410 (834 upregulated and 576 downregulated) and 192 (162 upregulated and 30 downregulated) genes displayed differential expression in 2 h macrophage-ingested *wt* and *Cgsnf2Δ*, compared to corresponding RPMI-grown cells (Figures 4A and 4B; Table S4). Similarly, 10 h macrophage-internalization led to the differential expression of 622 (482 upregulated and 140 downregulated) and 212 (155 upregulated and 57 downregulated) genes in *wt* and *Cgsnf2Δ*, respectively (Table S4), indicating that the magnitude of *Cg* transcriptional response to the macrophage milieu is dependent upon CgSnf2. Consistently, of all DEGs, only 42 genes were found to be CgSnf2-independent (Figure 4C). Of note, compared to *wt*, DEGs in *Cgsnf2Δ* were 7-fold and 3-fold less, upon 2 h and 10 h of macrophage internalization, respectively, indicating that CgSnf2 probably is more important for the initial global transcriptional response to the macrophage environment.

DAVID functional analysis revealed the enrichment of fatty acid β-oxidation (FAO) and TCA cycle GO terms, in addition to other terms, in upregulated gene sets in 2 h and 10 h macrophage-internalized *wt* (Table S5). Contrarily, while rRNA processing, translational frameshifting and ribosome biogenesis terms were enriched in downregulated genes in 2 h macrophage-internalized *wt*, 10 h macrophage internalization led to the downregulation of *de novo*' IMP biosynthetic process, DNA replication and iron ion homeostasis (Table S5). These data are consistent with the earlier microarray-based studies reporting similar gene expression patterns for macrophage-internalized *Cg*[14,20] and underscore

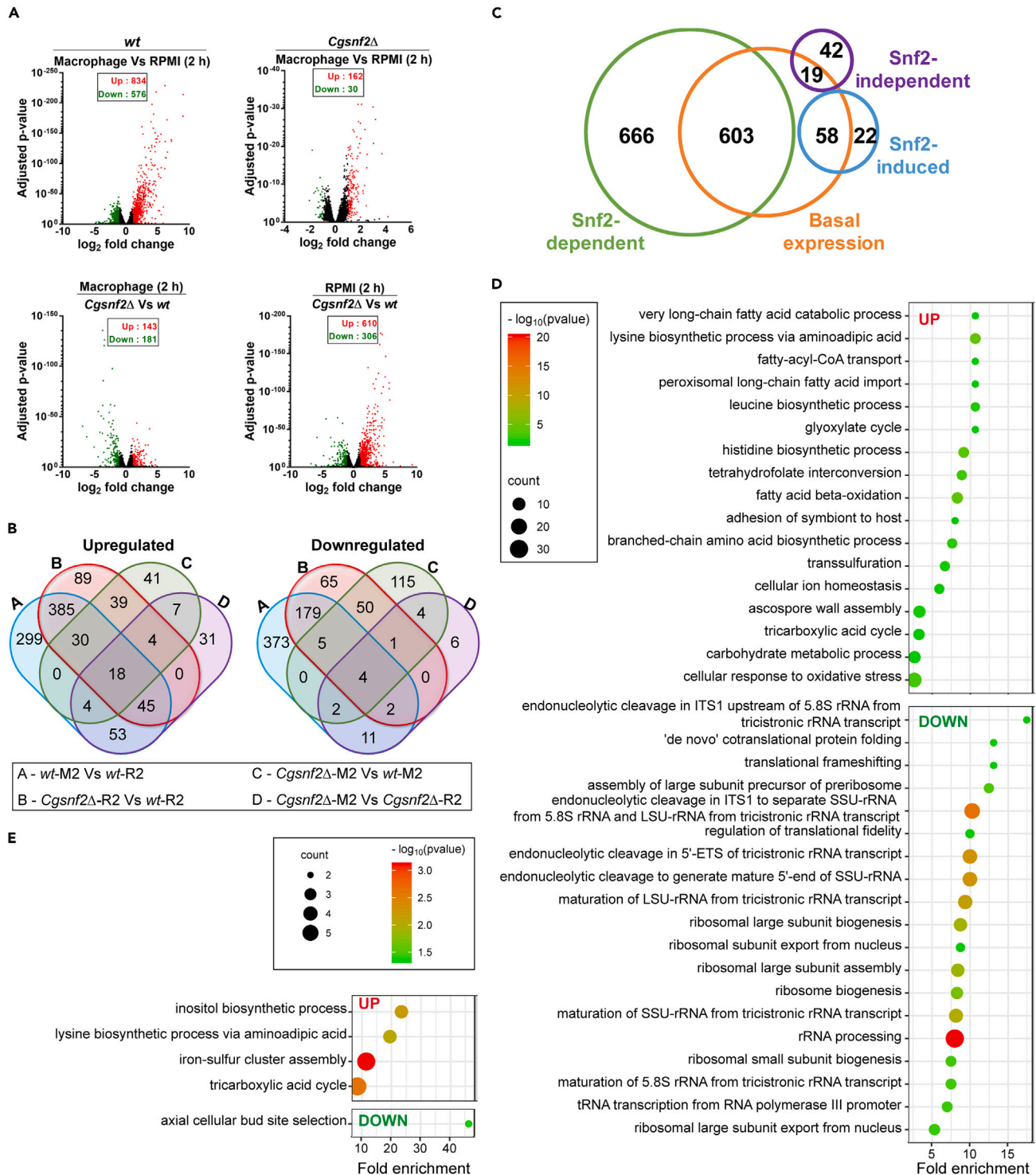**Figure 4. CgSnf2 is required for *Cg* transcriptional response to the macrophage environment**

(A) Volcano plots showing mean fold change of differentially expressed genes (DEGs) and their adjusted p (false discovery rate-corrected) values. Red, green and black dots indicate upregulated, downregulated and non-DEGs, respectively.

(B) Venn diagrams showing overlap in DEGs among four compared datasets.

Figure 4. *Continued*

(C) Venn diagram illustrating overlap in CgSnf2-regulated genes in 2 h RPMI-grown or 2 h macrophage-internalized *Cg*. Of 1410 DEGs in macrophage-internalized *wt*, expression of 1269 (90%) and 61 (4.3%) genes are dependent and independent of CgSnf2, respectively, with CgSnf2 regulating the basal expression of 680 (48%) genes. Additionally, the induction of 80 *Cg* genes (5.7%) in macrophages require CgSnf2.

(D and E) Bubble plots showing enriched GO-BP terms for upregulated and downregulated genes in 2 h RPMI-grown *Cgsnf2Δ* (D) and 2 h macrophage-internalized *Cgsnf2Δ* (E), compared to 2 h RPMI-grown *wild-type* and 2 h RPMI-grown *Cgsnf2Δ*, respectively.

See also Figure S5; Tables S4 and S5.

reprogramming of the carbon metabolism and shutting down of the translational machinery as characteristic components of the *Cg* transcriptional response to the macrophage environment.

Notably, CgSnf2's role in gene expression is unknown. Our comparison of 2 h RPMI-grown *wt* and *Cgsnf2Δ* transcriptomes revealed that *CgSNF2* deletion led to the upregulation of genes involved in FAO, TCA cycle, glyoxylate cycle, and adhesion of symbiont to host processes, and downregulation of genes implicated in rRNA processing, translational frameshifting and ribosome biogenesis processes (Figure 4D; Table S5). Since this transcriptional signature is hallmark of 2 h macrophage-internalized *wt*, it could partly account for the muted-transcriptional response of *Cgsnf2Δ* to macrophage ingestion. Further, the "fungal-type cell wall organization" term was enriched in upregulated genes in 10 h RPMI-grown *Cgsnf2Δ*, compared to the corresponding *wt* (Table S5). We verified the physiological relevance of this observation by performing cell wall component analysis, and found elevated β-glucan and chitin content in *Cgsnf2Δ* (Figure S4G), which suggests that CgSnf2 aids in cell wall composition maintenance probably by regulating the expression of cell wall organization genes.

Further, *Cgsnf2Δ* responded to 2 h of macrophage-ingestion by upregulating the iron-sulfur cluster assembly, TCA cycle, and inositol biosynthetic process, and downregulating the axial cellular bud site selection process (Figure 4E; Table S5). Notably, TCA cycle and translational frameshifting were upregulated and downregulated, respectively, in 10 h macrophage-internalized *Cgsnf2Δ* (Table S5). These gene expression data collectively suggest that like *wt*, *Cgsnf2Δ* reconfigures carbon metabolism, upon macrophage ingestion, however, it is deficient in closing down the translational machinery, probably because of already downregulated translation genes.

Chromatin dynamics in macrophage-internalized *wild type* correlates with CgSnf2-dependent transcriptional regulation

To determine if *Cg* nucleosome patterns correlate with the macrophage milieu-induced gene expression changes, we sought to integrate our MNase-Seq and RNA-Seq data. Snf2 in *S. cerevisiae* was recently shown to regulate the +1 nucleosome [transcription start site (TSS)-associated] position on the multidrug transporter-encoding *PDR5* gene, with both *S. cerevisiae* and *C. glabrata snf2Δ* mutants showing increased sensitivity to azole drugs.[24] Therefore, to examine if DEGs in macrophage-internalized *wt* exhibit +1 nucleosome position shifts, we first identified +1 nucleosomes in all four datasets, using the distance criterion of +1 to +220 bps between the TSS and the nucleosome center (Figure 5A; Table S6). Of 4215–4527 identified +1 nucleosomes, 10–20% showed altered position, occupancy, or fuzziness (Figure 5B). Transcriptome-nucleosome dynamics comparative analysis revealed that 8–16% DEGs contain dynamic nucleosomes at +1 position (Figure 5B; Table S6). Importantly, comparative analysis of 2 h RPMI-grown and 2 h macrophage-internalized *Cg* revealed that of 168 DEGs with dynamic +1 nucleosomes, 16 and 152 were differentially expressed in both macrophage-internalized *wt* and *Cgsnf2Δ*, and uniquely in macrophage-internalized *wt*, respectively (Figures 5B and 5C). Similarly, 80% of total DEGs with dynamic +1 nucleosomes were specific to 10 h macrophage-internalized *wt* compared to 10 h RPMI-grown *wt* (Figures 5B and 5D), underscoring the CgSnf2 requirement for DEGs regulation in macrophages. This inference was further strengthened by the comparison of 10 h/2 h RPMI-grown and 10 h/2 h macrophage-internalized *Cg*, wherein 57% and 84% of DEGs showed +1 nucleosome dynamics, respectively (Figure 5B). These results also suggest that +1 nucleosome dynamics (position shift and occupancy changes)-associated gene expression is majorly regulated by CgSnf2 in macrophages, and CgSnf2 in conjunction with other CRCs in RPMI medium. Intriguingly, functional analysis revealed the enrichment of the GO-BP terms, adhesion of symbiont to host and cell-abiotic substrate adhesion, in uniquely upregulated genes in *wt* with +1 dynamic nucleosomes in 2 h macrophage-internalized/2 h RPMI-grown and 10 h macrophage/2 h macrophage-internalized compared datasets, respectively (Figures 5E and 5F). Only one GO-BP term was enriched in uniquely differentially-expressed genes in *wt* with +1 dynamic nucleosomes for other two datasets, viz., "mitochondrial electron transport, ubiquinol to cytochrome *c*" in 10 h macrophage-internalized/10 h RPMI-grown, and "transcription-dependent tethering of RNA polymerase II gene DNA at nuclear periphery" in 10 h RPMI/2 h RPMI-grown datasets. Altogether, these data suggest that the macrophage milieu-induced, CgSnf2-mediated +1 nucleosome reconfiguration in *Cg* may contribute to the transcriptional regulation of cell surface adhesin genes.

CgSnf2-dependent *EPA1* regulation is pivotal to the *C. glabrata*-mediated suppression of IL-1β secretion in macrophages

In line with the above findings, comparative transcriptome analysis of 2 h macrophage-ingested *Cgsnf2Δ* and *wt* revealed the upregulation of genes involved in adhesion of symbiont to host and fungal-type cell wall organization BPs in the mutant (Table S5), pointing toward a possible role for cell wall remodeling in *Cg*-macrophage interplay. Consistently, contrary to *wt*, 2 h macrophage-internalized *Cgsnf2Δ* showed no activation of the seven mannosyltransferase gene-containing cluster (*CgMT-C*), which included five β-1,2-mannosyltransferase-encoding genes, *CgBMT2-6*, and two α-1,3-mannosyltransferase-encoding genes, *CAGL0B02981g* and *CAGL0B03014g* (Figures S5A–S5C). Of note, mannosyltransferases in *C. albicans* mediate the mannosylation of the cell wall phosphopeptidomannan, phospholipomannan, and mannoproteins, with β-mannan being involved in *C. albicans* recognition by immune cells,[31] while CgBmt2-6 are required for gut colonization in the murine colitis model.[32]

A

Condition	+1 nucleosomes identified	+1 nucleosome dynamics		
		Position	Occupancy	Fuzziness
M2 Vs R2	4521	416	256	0
M10 Vs R10	4277	257	148	0
M10 Vs M2	4527	763	146	0
R10 Vs R2	4215	474	144	1

B

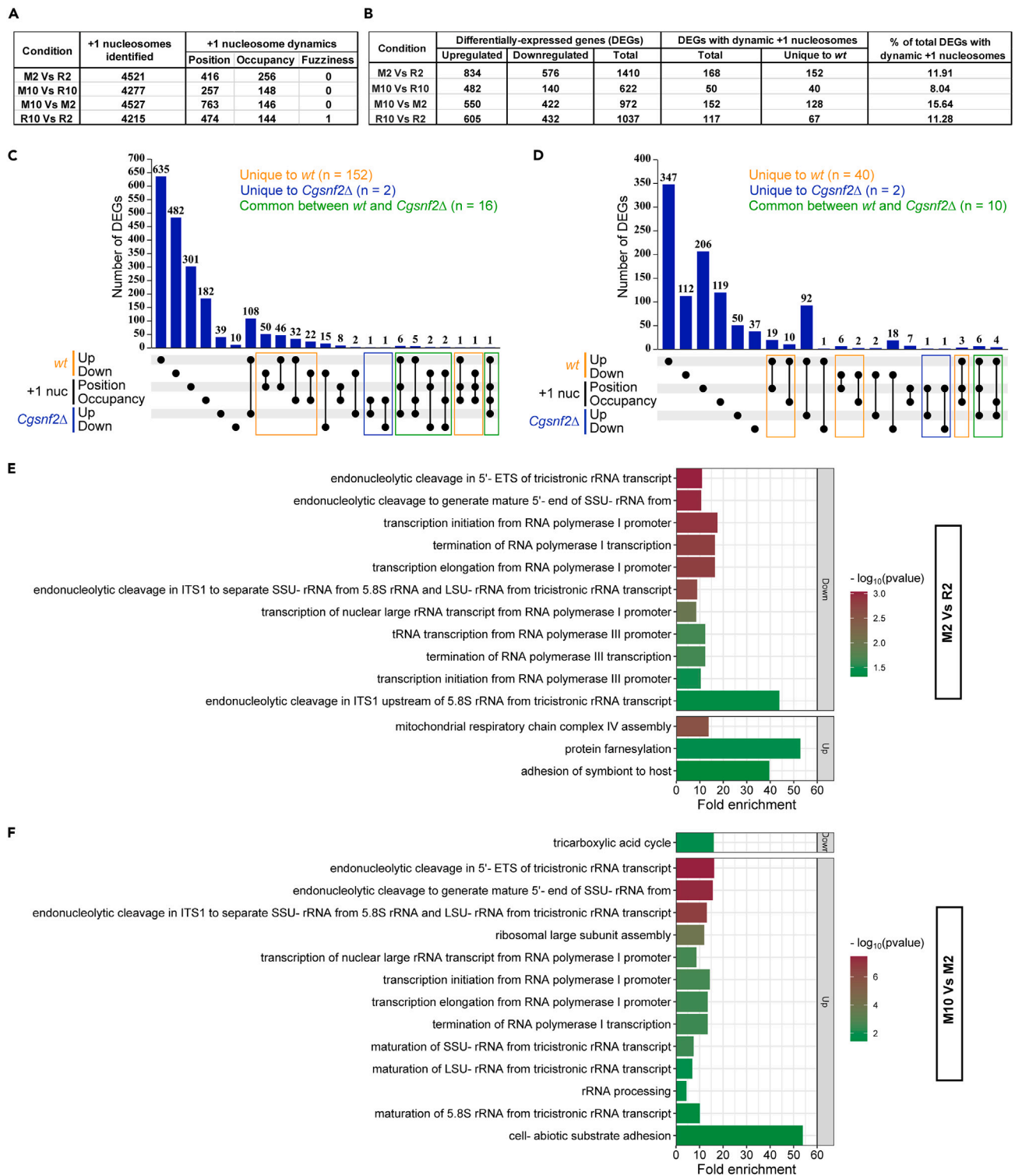| Condition	Differentially-expressed genes (DEGs)			DEGs with dynamic +1 nucleosomes		% of total DEGs with dynamic +1 nucleosomes
	Upregulated	Downregulated	Total	Total	Unique to *wt*	
M2 Vs R2	834	576	1410	168	152	11.91
M10 Vs R10	482	140	622	50	40	8.04
M10 Vs M2	550	422	972	152	128	15.64
R10 Vs R2	605	432	1037	117	67	11.28

C

D

E

F

Figure 5. CgSnf2-dependent transcriptional regulation is associated with nucleosome dynamics

(A) Total number of identified +1 dynamic nucleosomes.

(B) DEGs containing +1 nucleosomes.

Next, we examined how *CgSNF2* loss impacts the expression of the cell wall adhesin-encoding genes, as *Cg* adherence to macrophages is the first step in its phagocytosis by macrophages. Of known 81 adhesins,[33] 21 adhesin genes, including 9 subtelomeric adhesin genes, were differentially expressed in *Cgsnf2Δ* (Figure 6A). Notably, some *EPA* (epithelial adhesin) genes are subjected to subtelomeric silencing owing to their location at chromosome ends, with CgSnf2 negatively affecting subtelomeric silencing.[29,34] CgSnf2 has also been reported to regulate *EPA1* and *EPA6* expression negatively and positively, respectively.[29]

Based on *CgMT-C* and adhesin gene expression data, we hypothesized that the perturbed transcriptional regulatory networks in *Cgsnf2Δ* may interfere with the macrophage-induced α- and β-mannan- and adhesin-dependent cell surface remodeling in *Cg*, which may lead to increased IL-1β production and *Cgsnf2Δ* death in macrophages. To test our hypothesis, we first confirmed *CgBMT2* upregulation in macrophage-internalized *wt* by qRT-PCR (Figure S5D). Next, we generated a mutant lacking all seven genes of the mannosyltransferase cluster, and found that *CgMT-C* deletion led to reduced intracellular proliferation and increased IL-1β secretion (Figures S5E and S5F). These phenotypes are unlikely to be due to the slow growth of *CgMT-CΔ*, as it had *wt*-like growth rate in the YPD medium (Figure S5G). These results suggest that β-1,2-, and α-1,3-oligomannosides in *Cg* cell wall aid in immune evasion.

Next, to examine the role of adhesins in immune escape, we selected *EPA1*, from all differentially-expressed adhesin genes, for further analysis primarily for 3 reasons: First, Epa1 is the major adhesin for *Cg* adherence to host cells.[35,36] Second, *EPA1*-expressing *S. cerevisiae* adhered well to macrophages and stimulated inflammatory cytokine production.[36] Third, the eleven aspartyl protease-deficient *Cgyps1-11Δ* mutant, with elevated surface-exposed Epa1, was killed in macrophages, due to increased IL-1β secretion.[14,17] We first verified RNA-Seq results by qRT-PCR. *EPA1* transcription was activated and repressed upon *CgSNF2* deletion and macrophage-internalization of *wt* cells, respectively (Figures 6B and 6C), thereby raising two possibilities: (1) *EPA1* downregulation aids in restraining the macrophage pro-inflammatory response, and (2) Increased *EPA1* expression is deleterious to *Cg* survival.

To address these, we performed five experiments. First, we overexpressed *EPA1* from the strong *PDC1* promoter in *wt* and profiled growth in THP-1 cells. We found *wt/EPA1* to display reduced proliferation (Figure 6D), and 3-fold increased IL-1β secretion in macrophages (Figure 6E). Since Epa1 is a calcium-dependent lectin, lactose treatment inhibits its binding to host asialo-lactosyl-containing carbohydrates.[35] Consistently, THP-1 infection with lactose-treated *wt/EPA1* cells reduced IL-1β secretion significantly (Figure 6E), reinforcing the role of Epa1 in modulating IL-1β production. Second, we deleted the *EPA1* gene in the *Cgsnf2Δ* background, and found that *Cgsnf2Δepa1Δ* infection invoked 1.5-fold less IL-1β production in THP-1 macrophages, compared to infection with the single *Cgsnf2Δ* mutant (Figure 6F). IL-1β secretion was similar in response to *wt* and *epa1Δ* infection, probably due to functional redundancy among Epa adhesins (Figure 6F). Third, we performed the same analysis with *Cgyps1-11Δ* after deleting *EPA1*, and found that *Cgyps1-11Δepa1Δ*-infected macrophages secreted 1.3-fold less IL-1β than *Cgyps1-11Δ*-infected cells (Figure 6G). Notably, CgYapsins are required for Epa1 processing from the cell wall, and *Cgyps1-11Δ* contained increased Epa1 levels in its cell wall.[14] Fourth, we checked the intracellular survival of *epa1Δ* in THP1-macrophages, and found *wt*-like intracellular proliferation, while *Cgsnf2Δepa1Δ* showed 27% better survival than *Cgsnf2Δ* (Figure 6H), highlighting Epa1's adverse contribution to *Cgsnf2Δ* survival in macrophages. Finally, FACS and immunofluorescence analysis revealed increased surface expression of Epa1 in *Cgsnf2Δ*, compared to *wt* (Figures 6I and S6A), linking Epa1 transcriptional activation with Epa1 surface exposure in *Cgsnf2Δ*. Of note, while the *wt*-like behavior of *epa1Δ* in THP1-macrophages probably reflects a robust system of functionally redundant adhesins, the substantial contribution of Epa1 to *Cgsnf2Δ* and *Cgyps1-11Δ* mutants' phenotypes could be due to deregulated expression/functions of other adhesins in these mutants.

Altogether, these data suggest that Epa1 is immunostimulatory, and acts as a fungal activator of IL-1β induction, and that *EPA1* levels are probably regulated transcriptionally by CgSnf2 via nucleosome repositioning, and post-translationally by CgYapsins via Epa1 processing off the cell wall.[14] Of note, since CgSnf2 is essential for diverse stress survival (Figure 2A), large-scale gene dysregulation in the *Cgsnf2Δ* mutant, due to global alterations in chromatin architecture, may contribute to phenotypes associated with *CgSNF2* deletion. However, increased IL-1β secretion and diminished intracellular replication, upon *EPA1* overexpression and *CgMT-C* deletion, underscore Epa1 and CgMT-C functions in immune escape mechanisms.

CgSnf2 binds to *EPA1* promoter

Next, to demonstrate that CgSnf2 directly regulates *EPA1* expression, we performed four experiments. First, through chromatin immunoprecipitation, we showed 2-fold enrichment of CgSnf2 on *EPA1* promoter (Figure 6J), suggesting that CgSnf2 keeps *EPA1* expression in check under normal growth conditions. Second, we determined nucleosome occupancy on *EPA1* promoter in *wt* and *Cgsnf2Δ* strains, and found it to be lower in the mutant (Figure 6K), indicating that increased *EPA1* expression in *Cgsnf2Δ* could partly be due to reduced nucleosome abundance at *EPA1* promoter. Third, we mutated the conserved serine (Ser-861) residue in the ATPase domain of CgSnf2 (Figures S6B and S6C) to aspartate. Despite good expression (Figure S6D), CgSnf2[S861D] could neither rescue stress susceptibility nor increased *EPA1* expression in *Cgsnf2Δ* (Figures S6E and F). Contrary to CgSnf2, CgSnf2[S861D] also did not abolish elevated IL-1β secretion in *Cgsnf2Δ*-infected macrophages (Figure S6G), underscoring CgSnf2 catalytic functions, and, by extension, the SWI/SNF complex-mediated chromatin remodeling, in
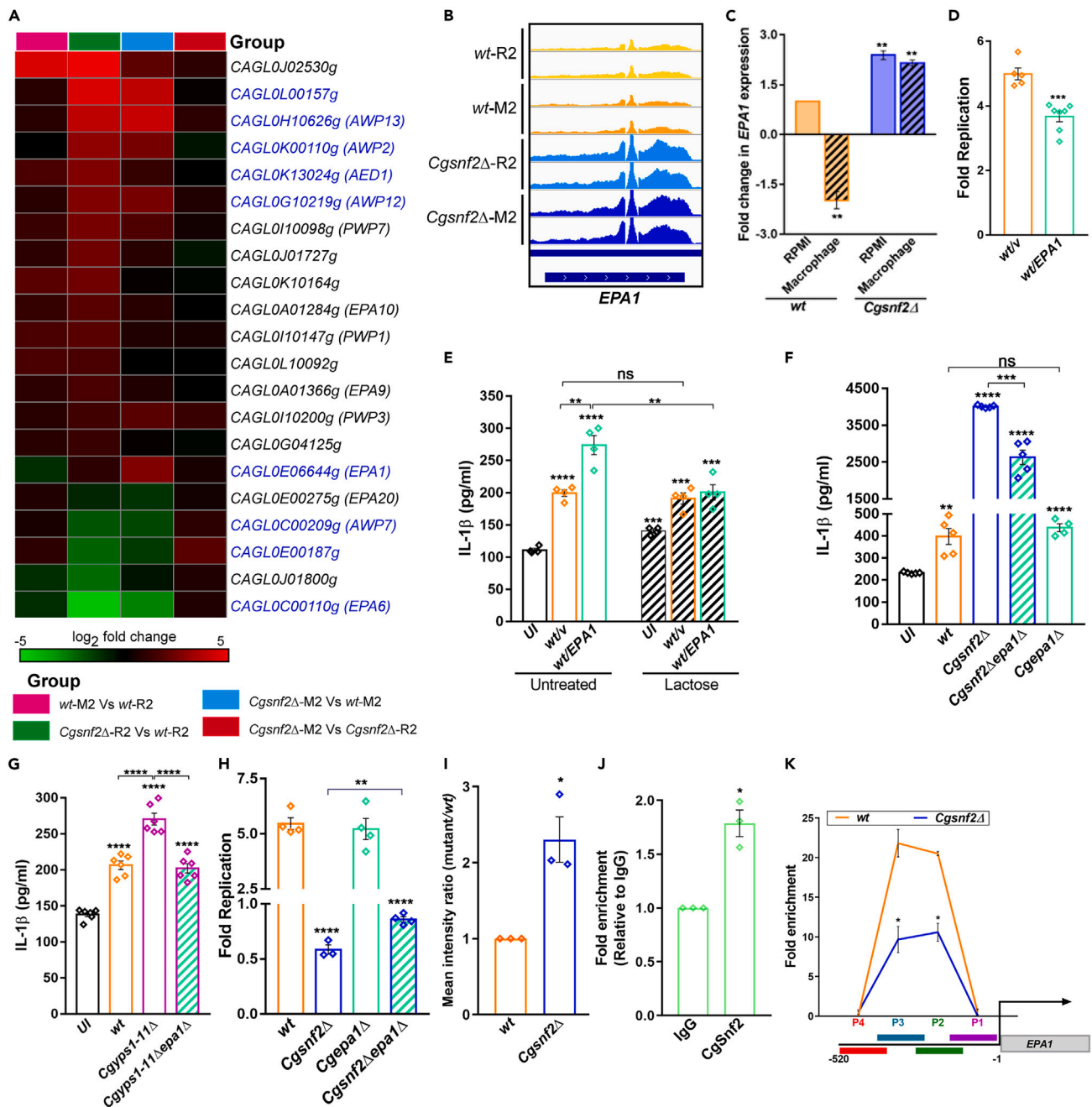
Figure 6. *EPA1* expression is deleterious for *Cg* survival in macrophages

(A) Heatmap shows the differential expression of 21 adhesin genes. Adhesin genes encoded at subtelomeric regions (25 kb from the chromosome ends) are marked in blue color. R2 and M2 refer to *Cg* grown in RPMI medium and infected to THP-1 macrophages for 2 h, respectively.

(B) Integrative genome viewer (IGV) snapshot of RNA-Seq signal at *EPA1* locus (ChrE: 682420 to 685524 bp). All IGV tracks have the same scaling factor [0–750] for the Y axis.

(C) qPCR-based analysis of *EPA1* expression after 2 h growth in RPMI medium or macrophage internalization. Data mean $\pm$ SEM (n = 3) were normalized with *ACT1* mRNA control, and plotted as fold change in gene expression, compared to RPMI-grown *wt* (considered as 1.0). **p $\leq$ 0.01; Paired two-tailed Student's t test.

(D) *Cg* replication in THP-1 macrophages. Data represent mean $\pm$ SEM (n = 5–7). ***p $\leq$ 0.005; Unpaired two-tailed Student's t test.

(E) IL-1β secretion in uninfected (UI) and *Cg*-infected THP-1 macrophages. *Cg* strains were either untreated- or treated with 10 mM lactose, 1 h prior to THP-1 infection, and the infection was continued for 24 h in the presence of lactose. Data represent mean $\pm$ SEM (n = 4). **p $\leq$ 0.01; ***p $\leq$ 0.005; ****p $\leq$ 0.001; Unpaired two-tailed Student's t test.

Figure 6. Continued

(F and G) IL-1β secretion in uninfected (UI) and *Cg*-infected THP-1 macrophages. Data represent mean ± SEM (n = 4–6). **p ≤ 0.01; ***p ≤ 0.005; ****p ≤ 0.001; Unpaired two-tailed Student's t test.

(H) *Cg* survival in THP-1 macrophages. Data represent mean ± SEM (n = 3–4). **p ≤ 0.01; ****p ≤ 0.001; Unpaired two-tailed Student's t test.

(I) FACS-based Epa1 surface expression analysis. Data represent mean ± SEM (n = 3). *p ≤ 0.05; Paired two-tailed Student's t test.

(J) ChIP-qPCR quantification of the level of bound, ectopically expressed SFB-tagged CgSnf2 to *EPA1* promoter. Y axis label is fold enrichment, with immunoglobulin G (IgG)-control and anti-FLAG (CgSnf2) antibodies. Data represent mean ± SEM (n = 3). *p ≤ 0.05; Paired two-tailed Student's t test.

(K) MNase-qPCR-based measurement of nucleosome occupancy at four indicated positions, P1, P2, P3 and P4, on *EPA1* promoter in 2 h RPMI-grown *wt* and *Cgsnf2Δ* cells. Data represent mean ± SD (n = 2). *p ≤ 0.05; Unpaired two-tailed Student's t test.

See also Figure S6.

Cg-mediated suppression of the host immune response. Fourth, we generated mutants lacking two other subunits of the SWI/SNF complex, CgSnf5 and CgSnf6. Like *Cgsnf2Δ*, *Cgsnf5Δ*, and *Cgsnf6Δ* were killed in THP-1 macrophages (Figure S6H), with both mutants also invoking elevated IL-1β secretion in macrophages (Figure S6I). Among *CgsnfΔ* mutants, *Cgsnf2Δ* grew most slowly (Figure S6J). However, the slow growth of *Cgsnf2Δ*, *Cgsnf5Δ*, and *Cgsnf6Δ* is unlikely to solely account for killing in macrophages, as the doubling time of *Cgsnf6Δ* is only 16% longer than that of *wt* in rich medium (Figure S6K). Altogether, these results unequivocally link the SWI/SNF complex with intracellular survival of, and immune evasion by *Cg*.

CgSnf2-dependent IL-1β restriction involves nuclear factor-kappa B signaling

NLRP3 inhibition in macrophages neither completely reversed IL-1β secretion nor *Cgsnf2Δ* killing (Figure 3), which could be due to other activated immune signaling pathways. Therefore, to define CgSnf2-repressed IL-1β-producing host signaling pathways, we focused on three pathways, nuclear factor-kappa B (NF-κB), phosphoinositide-3-kinase (PI3K)-protein kinase B/Akt (Akt) and p38 mitogen-activated protein kinase (MAPK) signaling pathways.[37–39] The NF-κB, a heterodimer of p50 and p65 proteins, is a transcriptional factor which regulates NLRP3 expression and controls the macrophage inflammatory gene expression.[40] Akt and p38 pathways are also implicated in antifungal immunity.[40] We found 1.8-, 2- and 10-fold higher phosphorylation of p65 (regulatory protein of NF-κB), Akt serine/threonine kinase (downstream effector of PI3K signaling), and p38 MAPK in *Cgsnf2Δ*-infected macrophages, compared to uninfected macrophages, respectively (Figures 7A, S7A and S7B). p65, Akt and p38 phosphorylation in *Cgsnf2Δ*-infected macrophages was also higher, compared to *wt*-infected macrophages (Figures 7A, S7A and S7B). Together, these results indicate a role for CgSnf2 in dampening the activation of three other host pathways.[37–39] Consistently, IL-1β levels were lower in BAY 11–7082 (blocks the inhibitory kappa B protein of NF-κB activation), SH-6 (Akt-specific inhibitor), and SB203580 (p38 inhibitor)-treated *Cgsnf2Δ*-infected macrophages, compared to untreated mutant-infected macrophages (Figures 7B, S7C and S7D). Further, *Cgsnf2Δ* infection also resulted in the elevated secretion of two other pro-inflammatory cytokines, TNF-α and IL-8, in macrophages, which were partially reversed by all immune signaling inhibitors, but for the NLRP3 inhibitor MCC950 (Figures 7C and 7D). These data suggest that *C. glabrata* impedes macrophage activation by controlling the inflammatory response via modulation of multiple signaling pathways.

Since fungal PAMP (pathogen-associated molecular pattern)-induced signaling pathways may converge on NF-κB activation, which is associated with p65 nuclear translocation,[40] we examined p65 cellular localization in J774A.1 macrophages, as these murine macrophage-like cells have larger cytosol volume. We found the 1.5-fold higher translocation of p65 to the nucleus (Figure 7E) in *Cgsnf2Δ*-infected, compared to *wt*-infected macrophages. Further, the role of Epa1 in the *Cg*-mediated restriction of the NF-κB pathway was demonstrated by enhanced and diminished nuclear translocation of p65 in J774A.1 macrophages infected with *EPA1*-overexpressing *Cg* (Figure 7E) and *Cgsnf2Δepa1Δ* cells (Figure 7E), respectively. Altogether, these data reveal a hitherto unknown facet of *Cg*-mediated host response modulation, via Epa1 adhesin, that involves the master transcriptional regulator, NF-κB, of the inflammatory response.

Finally, to investigate if the NF-κB-dependent inflammatory response represents a pan anti-*Candida* response of macrophages, we infected THP-1 cells with four *Candida* species, *Cg*, *C. albicans*, *C. auris,* and *C. tropicalis*. We found increased IL-1β production in all infections, which was reduced upon treatment with BAY 11–7082 (Figure 7F), indicating that NF-κB governs the macrophage inflammatory response against *Candida* pathogens. Notably, *S. cerevisiae* infection of THP-1 cells invoked no IL-1β secretion (Figure S7E). Altogether, these data indicate that macrophages respond to pathogenic *Candida* yeasts via IL-1β production, and that the controlled augmentation of IL-1β can potentially be useful for host-directed anti-*Candida* therapy.

DISCUSSION

Cg resides on mucosal surfaces in healthy humans but causes superficial mucosal and life-threatening invasive infections in immunocompromised patients.[41] Macrophages constitute key host immune defense cells against candidemia, with fungal cell wall structural components, β-glucan and mannan, involved in immune recognition.[42] Here, we present the first genome-wide nucleosome landscape of macrophage-internalized *Cg*, and establish CgSnf2 as a key determinant of fungal immune evasion. We show that *Cg* modulates NF-κB signaling, by regulating the expression of probable host-recognizable immunostimulatory Epa1 adhesin and immunosuppressive β-1,2- oligomannosides, via CgSnf2, to subvert pro-inflammatory cytokine production in macrophages.

The active immune suppression mechanisms in *Cg* are poorly understood, and involve impeding phagolysosome acidification and subverting Syk-dependent IL-1β production.[17,20] The cell wall of *Cg* is the first point-of-contact with the host, and is a multilayered organelle consisting of an inner structural network of chitin, immunostimulatory β-1,3-glucan and β-1,6-glucan, and the outer mannan layer, which is comprised of N-linked
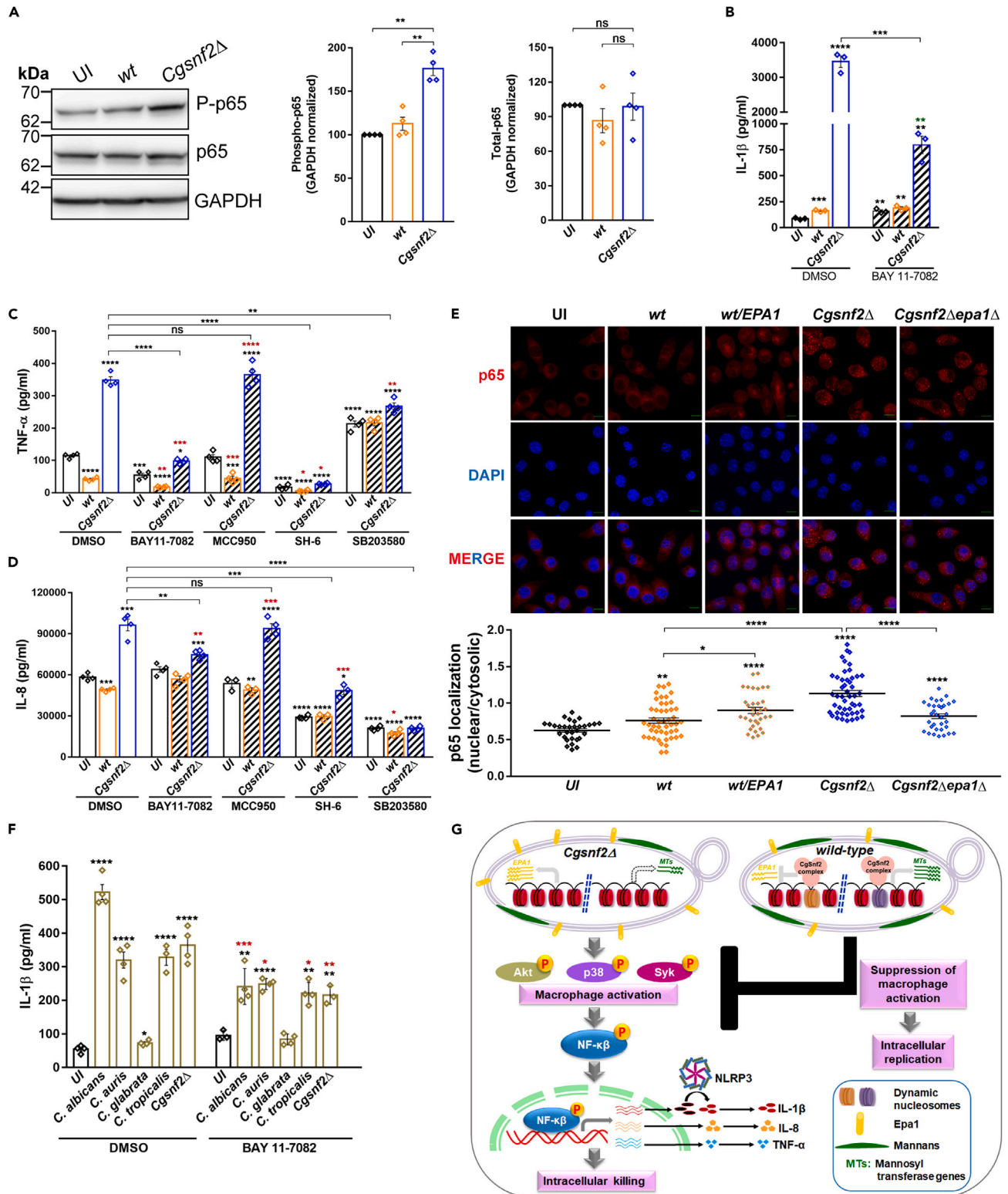
Figure 7. *EPA1* expression governs the nuclear localization of NF-κB

(A) Representative western blots of phosphorylated p65 expression. Bar graphs show fold change in phosphorylation, normalized to GAPDH signal. Data represent mean ± SEM (n = 4). **p ≤ 0.01; Paired two-tailed Student's t test.

Figure 7. Continued

(B) IL-1β in uninfected (UI) and *Cg*-infected THP-1 macrophages which were treated with DMSO or NF-κB inhibitor (BAY 11–7082; 10 μM). **p ≤ 0.01; ***p ≤ 0.005; ****p ≤ 0.001; Unpaired two-tailed Student's t test. Black and green asterisks represent statistically significant differences in IL-1β levels, compared to DMSO-treated uninfected and BAY 11-7082-treated uninfected macrophages, respectively.

(C and D) TNF-α (C) and IL-8 (D) secretion in uninfected (UI) and *Cg*-infected THP-1 macrophages which were treated with DMSO, BAY 11–7082 (10 μM), NLRP3 inhibitor (MCC950; 15 μM), Akt inhibitor (SH-6; 5 μM) or p38 MAPK inhibitor (SB203580; 10 μM). Data represent mean ± SEM (n = 3–4). *p ≤ 0.05; **p ≤ 0.01; ***p ≤ 0.005; ****p ≤ 0.001; Unpaired two-tailed Student's t test. Black and red asterisks represent statistically significant differences in TNF-α and IL-8 levels, compared to DMSO-treated uninfected and the corresponding inhibitor-treated uninfected macrophages, respectively.

(E) Confocal images show the cellular localization of p65 in uninfected or *Cg*-infected J774A.1 cells, as detected with anti-p65 antibody. DAPI was used to stain the macrophage nuclei. Bar = 10 μm. The p65 signal was quantified using ImageJ, and data represent (mean ± SEM; n = 30–50 cells) ratio of nuclear to cytosolic p65. *p ≤ 0.05; **p ≤ 0.01; ****p ≤ 0.001; Unpaired two-tailed Student's t test.

(F) IL-1β secretion in DMSO or BAY 11–7082 (10 μM)-treated uninfected (UI) THP-1 and THP-1 cells infected with four *Candida* species, *C. albicans*, *C. auris*, *C. glabrata* and *C. tropicalis*, at a MoI of 5:1 for 4 h. Data represent mean ± SEM (n = 3–4). *p ≤ 0.05; **p ≤ 0.01; ***p ≤ 0.005; ****p ≤ 0.001; Unpaired two-tailed Student's t test. Black and red asterisks represent statistically significant differences in IL-1β levels, compared to DMSO-treated uninfected and respective DMSO-treated *Candida spp*-infected THP-1 macrophages, respectively.

(G) A schematic illustrating how CgSnf2 ATPase-mediated chromatin remodeling, during *Cg*-macrophage interaction, results in cell surface reconfiguration, and aids *Cg* suppress signaling pathways in host macrophages.

See also Figure S7; Table S1.

or O-linked mannosylated proteins, and is presumed to shield the inner core from immune cells.[4,42] Dectin-1, Dectin-2, mannose, TLR4, galectin 3 and TLR9 receptors are involved in β-1,3-glucan, α-mannan, mannan and mannoprotein, O-linked mannan, β-mannan, and chitin and DNA recognition, respectively.[42] Epa1, a founding member of the Epa-adhesin family, is a GPI-anchored, glucan cross-linked, calcium-dependent adhesin, possesses an N-terminal PA14 ligand-binding domain, and resides in the outer layer of the cell wall.[35,43,44] Epa1 is shaved off the cell wall in CgYapsins-dependent manner.[14] Epa1 binds to host glycan ligands containing terminal galactose residue, and mediates adhesion to host epithelial, endothelial, and macrophage cells.[35,36,44,45] Our data establish Epa1 as a fungal PAMP, whose finely tuned expression is pivotal to restrain the pro-inflammatory innate immune response. Notably, *EPA1* overexpression, due to gain-of-function mutation in CgPdr1 transcriptional activator, was associated with decreased *Cg* phagocytosis by macrophages in a *Cg* strain-dependent manner, and increased adherence to epithelial cells in all *Cg* strain backgrounds,[46] underscoring two distinct roles for Epa1 in host-*Cg* interaction. Both *wt* and *Cgsnf2Δ* displayed ~100% phagocytosis rate which is consistent with CgPdr1 mutation-dependent *EPA1* overexpression not affecting the internalization of its parent strain, BG2.[46] Further, since Epa1 binding to NKp46 receptor led to *Cg* killing in natural killer cells,[47] the decrease in surface-exposed Epa1 is likely to constitute a principal *Cg* defense strategy against multiple immune cell-types.

CgSnf2 regulates both basal and macrophage milieu-responsive expression of *EPA1* and other adhesin genes. *Cg* possesses 81 adhesins, with many adhesin genes encoded at subtelomeric regions.[33,44] Nicotinic acid limitation relieves subtelomeric adhesin gene silencing, as restricted NAD⁺ availability reduces the activity of the NAD⁺-dependent histone deacetylase Sir2.[44,48] Expression of *EPA1*, which is localized 25 kb away from the right telomere of chromosome E, is negatively regulated by the subtelomeric silencing-protein complex, protosilencer Sil2126 and a negative-sequence element.[44] We add another regulatory layer of CgSnf2-dependent chromatin remodeling to *EPA1* transcription control which may involve +1 nucleosome position shift, as evidenced in a 60 bp shift toward the *EPA1* gene body in 2 h macrophage-internalized *Cg*, compared to RPMI-grown *Cg* (Figure S7F). Additionally, we observed nucleosome compaction at the *EPA1* promoter and the 3′ UTR in macrophage-internalized *Cg*, with the average internucleosomal distance being 206 bp and 177 bp in RPMI-grown and macrophage-internalized *Cg*, respectively (Figure S7G). This complex Epa1 regulation could be pivotal to induce *EPA1* expression for initial infection stages involving *Cg* adherence to host epithelial and endothelial cells, and repress *EPA1* transcription later to evade immune recognition and activation. Consistently, early Syk inhibition, following *Cg* ingestion, is pivotal to control *Cg* proliferation effectively in macrophages,[49] and the timely fungal immunogenic molecule-masking and unmasking aids in manipulating immune responses.[50]

Based on our findings, we speculate that in the absence of the hyphal form, *Cg* may primarily rely on CgSnf2-dependent dynamic cell surface organization to avoid immune sentinel cells (Figure 7G). Accordingly, RNAPII ChIP-Seq analysis revealed that *Cg* adhesin genes were upregulated and downregulated, marking immediate (30 min) and late (2 h onwards) response, respectively, to macrophage infection, with CgSnf2 being transcriptionally downregulated at 30 min post-infection.[51] This study also reported 1589 genes to be either constitutively expressed or temporally induced in macrophage-internalized *Cg*,[51] which is similar to 1410 DEGs, we identified in 2 h macrophage-ingested *Cg*. Our data suggest that macrophage activation, in response to *Cg* infection, is likely attained by multiple immune signaling pathways. Consistently, loss of the Dectin-1 or Dectin-2 (α-mannan receptor)-mediated Syk signaling individually had no effect on *Cg* replication in macrophages.[49] Altogether, although our data unequivocally show the epigenetic regulation of *Cg* immunomodulatory factors, the nature and distribution of these PAMPs (cell wall-associated or shedded Epa1; α- or β-mannosides), and their immune receptors remain to be identified. Similarly, whether and how Epa1 and mannosides co-operate to antagonize immune-signalling pathways, thereby generating *Cg*-specific immune evasion mechanisms, warrant further studies.

Microbial pathogens often employ heterochromatin structure to control virulence gene expression,[30] and nucleosome position changes regulate stress-response genes, with growth and stress-gene promoters exhibiting distinct chromatin features in hemiascomycetous yeasts, including *Cg*.[28] *Cg* dynamically switches its chromatin between transcriptionally active euchromatin and transcriptionally silent heterochromatin.[20] We mapped 86–102 nucleosomes to the 18.64 kb mannosyl transferase gene-cluster region under R2, M2, R10 and M10 conditions, with 4–22% nucleosomes exhibiting altered occupancy or position (Tables S1 and S2). Additionally, an increased occupancy at +1 and −2

nucleosomes for *CgBMT5*, and a 90 bp shift toward TSS was observed for the *CAGL0B02981*g gene, in 2 h macrophage-internalized *Cg* (Figure S7H). Notably, the dynamic nucleosome number at *CgMT-C* loci was 3- to 6-fold lower in 10 h macrophage-internalized/10 h RPMI-grown *Cg*, compared to the other three datasets (Table S2). Altogether, these results implicate nucleosome dynamics in controlling *CgMT-C* gene expression, though the significance of observed nucleosome position and occupancy changes remains to be determined. Overall, our data also raise the possibility that the nucleosome pattern on immunomodulatory genes in pathogenic fungi may differ from the gene-averaged nucleosome pattern, which can potentially be useful for therapeutic interventions.

CRCs remodel chromatin by changing the composition of, mobilizing, or evicting nucleosomes.[22] *Cg* has seven ATP-dependent CRCs, of which the RSC complex ATPase CgSth1 may be essential for *Cg* growth. Since 59% of DEGs in macrophage-internalized *Cg* contained CgRsc3-binding sites,[20] multiple chromatin remodellers may direct nucleosome position. Identifying genomic loci with repositioned/shifted nucleosomes in macrophage-internalized *Cgrsc3aΔbΔ* and *Cgsnf2Δ* mutants, and genome-wide mapping of CgSnf2 and CgSth1, will unveil individualistic CRC contribution. However, given CgSnf2's essentiality for intracellular survival, its ability to create facile-chromatin regions and recruit specific transcription factors and/or RNAPII machinery may contribute majorly to *Cg* immune evasion.

In conclusion, chromatin reorganization in *Cg* impacts macrophages' inflammatory response and *Cg* survival. Due to CgSnf2 indispensability for immune evasion, exploring fungal-specific subunits of the SWI/SNF complex including Snf6[23] as new therapeutic targets holds promise. Toward this end, a chemical library screen to identify molecules targeting either fungal-specific SWI/SNF complex subunits or specifically Snf2 is likely to be beneficial. Additionally, the genome-wide nucleosome map of macrophage-internalized *Cg* will be a useful tool to delineate transcriptional changes arising from chromatin remodeling from those stemming from other gene expression regulatory mechanisms.

Limitations of the study

The current study has two key limitations. First, we could not examine nucleosome dynamics in macrophage-internalized *Cgsnf2Δ* cells. Second, our findings are not extended to mice lacking various immune cell receptors that recognize fungi and control fungal infections. Future studies could include *wt* and *Cgsnf2Δ* infections of receptor-deficient mice as well as macrophages isolated from these mice to identify the immune receptor/s involved in host defense against *Cg*.

STAR★METHODS

Detailed methods are provided in the online version of this paper and include the following:

- KEY RESOURCES TABLE
- RESOURCE AVAILABILITY
  - ○ Lead contact
  - ○ Materials availability
  - ○ Data and code availability
- EXPERIMENTAL MODEL AND STUDY PARTICIPANT DETAILS
  - ○ Animals
  - ○ Yeast strains
  - ○ Cell lines and primary cells
  - ○ Study approval
- METHOD DETAILS
  - ○ Strains, plasmids and growth conditions
  - ○ Growth analysis
  - ○ Biofilm formation assay
  - ○ Mice infection analysis
  - ○ *Cg*-macrophage interaction analysis
  - ○ Nucleosome dynamics analysis by MNase-Seq
  - ○ Immunoblotting analysis
  - ○ *Cg* cell wall analysis
  - ○ RNA-Sequencing analysis
  - ○ Imaging analysis
  - ○ Quantitative RT-PCR (qRT-PCR) analysis
  - ○ Chromatin immunoprecipitation (ChIP) analysis
  - ○ Nucleosome density analysis
  - ○ Functional enrichment analysis
- QUANTIFICATION AND STATISTICAL ANALYSIS

SUPPLEMENTAL INFORMATION

Supplemental information can be found online at https://doi.org/10.1016/j.isci.2024.109607.

AUTHOR CONTRIBUTIONS

KK conceived the study. KK and RK designed the study. KK and AP performed experiments and acquired data. KK, AP and RK analyzed data. KK prepared tables and figures. KK and RK wrote the article with inputs from AP.

DECLARATION OF INTERESTS

The authors declare no competing interests.

REFERENCES

1. Bongomin, F., Gago, S., Oladele, R.O., and Denning, D.W. (2017). Global and Multi-National Prevalence of Fungal Diseases—Estimate Precision. J. Fungi 3, 57. https://doi.org/10.3390/jof3040057.

2. Chakrabarti, A. (2015). Candida glabrata candidemia. Indian J. Crit. Care Med. 19, 138–139. https://doi.org/10.4103/0972-5229.152753.

3. Pfaller, M.A., Diekema, D.J., Turnidge, J.D., Castanheira, M., and Jones, R.N. (2019). Twenty Years of the SENTRY Antifungal Surveillance Program: Results for Candida Species From 1997-2016. Open Forum Infect. Dis. 6, S79–S94. https://doi.org/10.1093/ofid/ofy358.

4. Rasheed, M., Battu, A., and Kaur, R. (2020). Host–pathogen interaction in Candida glabrata infection: current knowledge and implications for antifungal therapy. Expert Rev. Anti Infect. Ther. 18, 1093–1103. https://doi.org/10.1080/14787210.2020.1792773.

5. Gabaldón, T., Martin, T., Marcet-Houben, M., Durrens, P., Bolotin-Fukuhara, M., Lespinet, O., Arnaise, S., Boisnard, S., Aguileta, G., Atanasova, I., et al. (2013). Comparative genomics of emerging pathogens in the Candida glabrata clade. BMC Genom. 14, 623. https://doi.org/10.1186/1471-2164-14-623.

6. Wisplinghoff, H., Bischoff, T., Tallent, S.M., Seifert, H., Wenzel, R.P., and Edmond, M.B. (2004). Nosocomial bloodstream infections in US hospitals: analysis of 24,179 cases from a prospective nationwide surveillance study. Clin. Infect. Dis. 39, 309–317. https://doi.org/10.1086/421946.

7. Gupta, A., Gupta, A., and Gupta, A. (2015). Candida glabrata candidemia : An emerging threat in critically ill patients. Indian J. Crit. Care Med. 19, 151–154. https://doi.org/10.4103/0972-5229.152757.

8. Meyahnwi, D., Siraw, B.B., and Reingold, A. (2022). Epidemiologic features, clinical characteristics, and predictors of mortality in patients with candidemia in Alameda County, California; a 2017-2020 retrospective analysis. BMC Infect. Dis. 22, 843. https://doi.org/10.1186/s12879-022-07848-8.

9. World Health Organization (2022). WHO Fungal Priority Pathogens List to Guide Research, Development and Public Health Action (WHO). https://www.who.int/publications/i/item/9789240060241.

10. Kumar, K., Askari, F., Sahu, M.S., and Kaur, R. (2019). Candida glabrata: A lot more than meets the eye. Microorganisms 7, 1–22. https://doi.org/10.3390/microorganisms7020039.

11. Kasper, L., Seider, K., and Hube, B. (2015). Intracellular survival of Candida glabrata in macrophages: immune evasion and persistence. FEMS Yeast Res. 15, fov042. https://doi.org/10.1093/femsyr/fov042.

12. Riedelberger, M., Penninger, P., Tscherner, M., Seifert, M., Jenull, S., Brunnhofer, C., Scheidl, B., Tsymala, I., Bourgeois, C., Petryshyn, A., et al. (2020). Type I Interferon Response Dysregulates Host Iron Homeostasis and Enhances Candida glabrata Infection. Cell Host Microbe 27, 454–466.e8. https://doi.org/10.1016/j.chom.2020.01.023.

13. Riedelberger, M., Penninger, P., Tscherner, M., Hadriga, B., Brunnhofer, C., Jenull, S., Stoiber, A., Bourgeois, C., Petryshyn, A., Glaser, W., et al. (2020). Type I Interferons Ameliorate Zinc Intoxication of Candida glabrata by Macrophages and Promote Fungal Immune Evasion. iScience 23, 101121. https://doi.org/10.1016/j.isci.2020.101121.

14. Kaur, R., Ma, B., and Cormack, B.P. (2007). A family of glycosylphosphatidylinositol-linked aspartyl proteases is required for virulence of Candida glabrata. Proc. Natl. Acad. Sci. USA 104, 7628–7633. https://doi.org/10.1073/pnas.0611195104.

15. Roetzer, A., Gratz, N., Kovarik, P., and Schüller, C. (2010). Autophagy supports Candida glabrata survival during phagocytosis. Cell Microbiol. 12, 199–216. https://doi.org/10.1111/j.1462-5822.2009.01391.x.

16. Seider, K., Brunke, S., Schild, L., Jablonowski, N., Wilson, D., Majer, O., Barz, D., Haas, A., Kuchler, K., Schaller, M., and Hube, B. (2011). The Facultative Intracellular Pathogen Candida glabrata Subverts Macrophage Cytokine Production and Phagolysosome Maturation. J. Immunol. 187, 3072–3086. https://doi.org/10.4049/jimmunol.1003730.

17. Rasheed, M., Battu, A., and Kaur, R. (2018). Aspartyl proteases in Candida glabrata are required for suppression of the host innate immune response. J. Biol. Chem. 293, 6410–6433. https://doi.org/10.1074/jbc.M117.813741.

18. Jacobsen, I.D., Brunke, S., Seider, K., Schwarzmüller, T., Firon, A., d'Enfért, C., Kuchler, K., and Hube, B. (2010). Candida glabrata persistence in mice does not depend on host immunosuppression and is unaffected by fungal amino acid auxotrophy. Infect. Immun. 78, 1066–1077. https://doi.org/10.1128/IAI.01244-09.

19. Willems, H.M.E., Lowes, D.J., Barker, K.S., Palmer, G.E., and Peters, B.M. (2018). Comparative analysis of the capacity of the candida species to elicit vaginal immunopathology. Infect. Immun. 86. e00527–18. https://doi.org/10.1128/IAI.00527-18.

20. Rai, M.N., Balusu, S., Gorityala, N., Dandu, L., and Kaur, R. (2012). Functional Genomic Analysis of Candida glabrata-Macrophage Interaction: Role of Chromatin Remodeling in Virulence. PLoS Pathog. 8, e1002863. https://doi.org/10.1371/journal.ppat.1002863.

21. Struhl, K., and Segal, E. (2013). Determinants of nucleosome positioning. Nat. Struct. Mol. Biol. *20*, 267–273. https://doi.org/10.1038/nsmb.2506.

22. Clapier, C.R., Iwasa, J., Cairns, B.R., and Peterson, C.L. (2017). Mechanisms of action and regulation of ATP-dependent chromatin-remodelling complexes. Nat. Rev. Mol. Cell Biol. *18*, 407–422. https://doi.org/10.1038/nrm.2017.26.

23. Tebbji, F., Chen, Y., Sellam, A., and Whiteway, M. (2017). The Genomic Landscape of the Fungus-Specific SWI/SNF Complex Subunit, Snf6, in Candida Albicans. mSphere *2*. https://doi.org/10.1128/mSphere.00497-17.

24. Nikolov, V.N., Malavia, D., and Kubota, T. (2022). SWI/SNF and the histone chaperone Rtt106 drive expression of the Pleiotropic Drug Resistance network genes. Nat. Commun. *13*, 1968. https://doi.org/10.1038/s41467-022-29591-z.

25. Chen, K., Xi, Y., Pan, X., Li, Z., Kaestner, K., Tyler, J., Dent, S., He, X., and Li, W. (2013). DANPOS: Dynamic analysis of nucleosome position and occupancy by sequencing. Genome Res. *23*, 341–351. https://doi.org/10.1101/gr.142067.112.

26. Huang, D.W., Sherman, B.T., and Lempicki, R.A. (2009). Systematic and integrative analysis of large gene lists using DAVID bioinformatics resources. Nat. Protoc. *4*, 44–57. https://doi.org/10.1038/nprot.2008.211.

27. Sherman, B.T., Hao, M., Qiu, J., Jiao, X., Baseler, M.W., Lane, H.C., Imamichi, T., and Chang, W. (2022). DAVID: a web server for functional enrichment analysis and functional annotation of gene lists (2021 update). Nucleic Acids Res. *50*, W216–W221. https://doi.org/10.1093/nar/gkac194.

28. Tsankov, A.M., Thompson, D.A., Socha, A., Regev, A., and Rando, O.J. (2010). The role of nucleosome positioning in the evolution of gene regulation. PLoS Biol. *8*, e1000414. https://doi.org/10.1371/journal.pbio.1000414.

29. Riera, M., Mogensen, E., d'Enfert, C., and Janbon, G. (2012). New regulators of biofilm development in Candida glabrata. Res. Microbiol. *163*, 297–307. https://doi.org/10.1016/j.resmic.2012.02.005.

30. Juárez-Reyes, A., and Castaño, I. (2019). Chromatin architecture and virulence-related gene expression in eukaryotic microbial pathogens. Curr. Genet. *65*, 435–443. https://doi.org/10.1007/s00294-018-0903-z.

31. Hall, R.A., and Gow, N.A.R. (2013). Mannosylation in Candida albicans: role in cell wall function and immune recognition. Mol. Microbiol. *90*, 1147–1161. https://doi.org/10.1111/mmi.12426.

32. Jawhara, S., Mogensen, E., Maggiotto, F., Fradin, C., Sarazin, A., Dubuquoy, L., Maes, E., Guérardel, Y., Janbon, G., and Poulain, D. (2012). Murine Model of Dextran Sulfate Sodium-induced Colitis Reveals Candida glabrata Virulence and Contribution of β-Mannosyltransferases. J. Biol. Chem. *287*, 11313–11324. https://doi.org/10.1074/jbc.M111.329300.

33. Xu, Z., Green, B., Benoit, N., Schatz, M., Wheelan, S., and Cormack, B. (2020). De novo genome assembly of Candida glabrata reveals cell wall protein complement and structure of dispersed tandem repeat arrays. Mol. Microbiol. *113*, 1209–1224. https://doi.org/10.1111/mmi.14488.

34. López-Fuentes, E., Gutiérrez-Escobedo, G., Timmermans, B., Van Dijck, P., De Las Peñas, A., and Castaño, I. (2018). Candida glabrata's genome plasticity confers a unique pattern of expressed cell wall proteins. J. Fungi *4*, 67. https://doi.org/10.3390/jof4020067.

35. Cormack, B.P., Ghori, N., and Falkow, S. (1999). An adhesin of the yeast pathogen Candida glabrata mediating adherence to human epithelial cells. Science *285*, 578–582. https://doi.org/10.1126/science.285.5427.578.

36. Kuhn, D.M., and Vyas, V.K. (2012). The Candida glabrata adhesin Epa1p causes adhesion, phagocytosis, and cytokine secretion by innate immune cells. FEMS Yeast Res. *12*, 398–414. https://doi.org/10.1111/j.1567-1364.2011.00785.x.

37. Cuadrado, A., and Nebreda, A.R. (2010). Mechanisms and functions of p38 MAPK signalling. Biochem. J. *429*, 403–417. https://doi.org/10.1042/BJ20100323.

38. Hoesel, B., and Schmid, J.A. (2013). The complexity of NF-κB signaling in inflammation and cancer. Mol. Cancer *12*, 1–15. https://doi.org/10.1186/1476-4598-12-86.

39. Manning, B.D., and Toker, A. (2017). AKT/PKB Signaling: Navigating the Network. Cell *169*, 381–405. https://doi.org/10.1016/j.cell.2017.04.001.

40. Patin, E.C., Thompson, A., and Orr, S.J. (2019). Pattern recognition receptors in fungal immunity. Semin. Cell Dev. Biol. *89*, 24–33. https://doi.org/10.1016/j.semcdb.2018.03.003.

41. Fidel, P.L., Vazquez, J.A., and Sobel, J.D. (1999). Candida glabrata: Review of epidemiology, pathogenesis, and clinical disease with comparison to C. albicans. Clin. Microbiol. Rev. *12*, 80–96. https://doi.org/10.1128/cmr.12.1.80.

42. Erwig, L.P., and Gow, N.A.R. (2016). Interactions of fungal pathogens with phagocytes. Nat. Rev. Microbiol. *14*, 163–176. https://doi.org/10.1038/nrmicro.2015.21.

43. Frieman, M.B., McCaffery, J.M., and Cormack, B.P. (2002). Modular domain structure in the Candida glabrata adhesin Epa1p, a β1,6 glucan-cross-linked cell wall protein. Mol. Microbiol. *46*, 479–492. https://doi.org/10.1046/j.1365-2958.2002.03166.x.

44. Timmermans, B., Peñas, A.D.L., and Castaño, I. (2018). Adhesins in Candida glabrata. Fungi J. 1–16. https://doi.org/10.3390/jof4020060.

45. Zupancic, M.L., Frieman, M., Smith, D., Alvarez, R.A., Cummings, R.D., and Cormack, B.P. (2008). Glycan microarray analysis of Candida glabrata adhesin ligand specificity. Mol. Microbiol. *68*, 547–559. https://doi.org/10.1111/j.1365-2958.2008.06184.x.

46. Vale-Silva, L.A., Moeckli, B., Torelli, R., Posteraro, B., Sanguinetti, M., and Sanglard, D. (2016). Upregulation of the Adhesin Gene EPA1 Mediated by PDR1 in Candida glabrata Leads to Enhanced Host Colonization. mSphere *1*. e00065–15. https://doi.org/10.1128/mSphere.00065-15.

47. Vitenshtein, A., Charpak-Amikam, Y., Yamin, R., Bauman, Y., Isaacson, B., Stein, N., Berhani, O., Dassa, L., Gamliel, M., Gur, C., et al. (2016). NK Cell Recognition of Candida glabrata through Binding of NKp46 and NCR1 to Fungal Ligands Epa1, Epa6, and Epa7. Cell Host Microbe *20*, 527–534. https://doi.org/10.1016/j.chom.2016.09.008.

48. Domergue, R., Castaño, I., De Las Peñas, A., Zupancic, M., Lockatell, V., Hebel, J.R., Johnson, D., and Cormack, B.P. (2005). Nicotinic acid limitation regulates silencing of Candida adhesins during UTI. Science *308*, 866–870. https://doi.org/10.1126/science.1108640.

49. Dagher, Z., Xu, S., Negoro, P.E., Khan, N.S., Feldman, M.B., Reedy, J.L., Tam, J.M., Sykes, D.B., and Mansour, M.K. (2018). Fluorescent Tracking of Yeast Division Clarifies the Essential Role of Spleen Tyrosine Kinase in the Intracellular Control of Candida glabrata in Macrophages. Front. Immunol. *9*, 1058. https://doi.org/10.3389/fimmu.2018.01058.

50. Cottier, F., Sherrington, S., Cockerill, S., del Olmo Toledo, V., Kissane, S., Tournu, H., Orsini, L., Palmer, G.E., Pérez, J.C., and Hall, R.A. (2019). Remasking of Candida albicans β-Glucan in Response to Environmental pH Is Regulated by Quorum Sensing. mBio *10*. e02347–19. https://doi.org/10.1128/mBio.02347-19.

51. Rai, M.N., Parsania, C., Rai, R., Shirgaonkar, N., Tan, K., Wong, K.H., Nandan, M., Ho, K., and Mo, W.-K.E. (2021). Temporal transcriptional response of Candida glabrata during macrophage infection reveals a multifaceted transcriptional regulator CgXbp1 important for macrophage response and drug resistance. Preprint at bioRxiv. https://doi.org/10.1101/2021.09.28.462173.

52. Schindelin, J., Arganda-Carreras, I., Frise, E., Kaynig, V., Longair, M., Pietzsch, T., Preibisch, S., Rueden, C., Saalfeld, S., Schmid, B., et al. (2012). Fiji: an open-source platform for biological-image analysis. Nat. Methods *9*, 676–682. https://doi.org/10.1038/nmeth.2019.

53. Kumar, K., Moirangthem, R., and Kaur, R. (2020). Histone H4 dosage modulates DNA damage response in the pathogenic yeast Candida glabrata via homologous recombination pathway. PLoS Genet. *16*, e1008620. https://doi.org/10.1371/journal.pgen.1008620.

54. Bhakt, P., Raney, M., and Kaur, R. (2022). The SET-domain protein CgSet4 negatively regulates antifungal drug resistance via the ergosterol biosynthesis transcriptional regulator CgUpc2a. J. Biol. Chem. *298*, 102485–102522. https://doi.org/10.1016/j.jbc.2022.102485.

STAR★METHODS

KEY RESOURCES TABLE

REAGENT or RESOURCE	SOURCE	IDENTIFIER
Antibodies		
Anti-Akt	Cell Signaling Technology	Cat#9272; RRID:AB_329827
Anti-Phospho-Akt (Ser473)	Cell Signaling Technology	Cat#9018; RRID:AB_2629283
Anti-p38 MAPK	Cell Signaling Technology	Cat#9228; RRID:AB_490886
Anti-Phospho-p38 MAPK	Cell Signaling Technology	Cat#4511; RRID:AB_2139682
Anti-p44/42 MAPK	Cell Signaling Technology	Cat#9102; RRID:AB_330744
Anti-Phospho-p44/42 MAPK	Cell Signaling Technology	Cat#4370; RRID:AB_2315112
Anti-p65	Cell Signaling Technology	Cat#8242; RRID:AB_10859369
Anti-Phospho-p65	Cell Signaling Technology	Cat#3033; RRID:AB_331284
Anti-Epa1	Cormack laboratory	N/A
Anti-FLAG	Sigma	Cat#F1804; RRID:AB_262044
Anti-GAPDH	Abcam	Cat#ab22555; RRID:AB_447153
Anti-rabbit	Cell Signaling Technology	Cat#7074; RRID:AB_2099233
Anti-mouse	Cell Signaling Technology	Cat#7076; RRID:AB_330924
Anti-Rabbit IgG (H+L), Alexa Fluor® 568 conjugate	Thermo Fisher Scientific	Cat#A-11011; RRID:AB_143157
Anti-Rabbit IgG (H+L), Alexa Fluor® 488conjugate	Abcam	Cat#ab150077; RRID:AB_2630356
Chemicals, peptides, and recombinant proteins		
MCC950	Calbiochem	538120
BAY 11-7082	Sigma	B5556
SH-6	Calbiochem	124009
SB 203580	Cell Signaling Technology	5633S
R406	MedChemExpress	HY-12067
Gel Extraction Kit	Qiagen	28706
PCR Purification Kit	Qiagen	28106
Miniprep Kit	Qiagen	27014
RNeasy Kit	Qiagen	74104
NTC (Nourseothricin)	Jena Bioscience	AB-102XL
Ampicillin	USB	11259
Phenylmethylsulphonyl fluoride	Amresco	754
Sodium fluoride	Merck	106449
Sodiumorthovanadate	Sigma	S6508
Protease inhibitor cocktail	Sigma	P8125
cOmplete protease inhibitor	Roche	4693132001
PhosSTOP phosphatase inhibitor	Roche	4906837001
Nonidet P-40	Roche	11754599001
PVDF Membranes	Amersham	10600023
Fat-free milk	Rockland	B501-0500
BSA (Bovine serum albumin)	Sigma	A2153
rProtein A-Sepharose	Cytiva	17127902

Continued

REAGENT or RESOURCE	SOURCE	IDENTIFIER
Taq Polymerase	Sigma	D1806
Phusion polymerase	ThermoFisher Scientific	F530
MNase	New England Biolabs	M0247S
BamHI	New England Biolabs	R3136S
SpeI	New England Biolabs	R3133L
XmaI	New England Biolabs	R0180L
XhoI	New England Biolabs	R0146L
DpnI	New England Biolabs	R0176L
T4 DNA ligase	New England Biolabs	M0202L
RNase cocktail	ThermoFisher Scientific	AM2286
DMSO (Dimethyl sulfoxide)	Sigma	D8418
PEG (Polyethylene Glycol)-3350	Sigma	88276
Lithium Acetate	Sigma	62393
Glass beads	Unigenetics	11079105
HU (Hydroxy urea)	Sigma	H8627
MMS (Methyl methanesulfonate)	Sigma	129925
H_2O_2 (Hydrogen peroxide)	Sigma	323381
MD (Menadione)	Sigma	M5625
β-ME (β-mercaptoethenol)	Sigma	M6250
DTT (Dithiothreitol)	Sigma	D0632
SDS	Sigma	62862
Caffeine	Himedia	RM1056
$CaCl_2$ (Calcium chloride)	Sigma	C5670
$MnCl_2$ (Manganese chloride)	Sigma	328146
$ZnCl_2$ (Zinc chloride)	Sigma	Z4875
$CuSO_4$ (Copper sulphate)	Himedia	RM6391
$FeCl_3$ (Ferric chloride)	Sigma	F2877
BPS (Bathophenanthrolinedisulfonic acid disodium salt hydrate)	Sigma	B1375
Glycerol	Sigma	G9012
Sodium acetate	Sigma	S2889
Oleic acid	Fisher Scientific	13295
Congo red	Sigma	C6767
FLC (Fluconazole)	Cipla	Forcan
Aniline blue	Himedia	GRM901
FITC-conjugated Concanavalin A	Sigma	C7642
CFW (Calcoflour white)	Sigma	F3543
Formaldehyde	Sigma	F8775
Zymolyase	Nacalai tesque	07663-91
Sorbitol	Sigma	S3889
Triton-X	Sigma	T8787
Tween 20	Sigma	P9416
Methanol	Qualigens	Q32407
Chloroform	Sigma	C2432
Tris	MP Biomedicals	2103133

(Continued on next page)

Continued

REAGENT or RESOURCE	SOURCE	IDENTIFIER
EDTA	Sigma	E6635
Glucose	BD Difco	215530
RPMI-1640	Gibco	21870076
DMEM	Gibco	10313021
PBS (Phosphate-buffered saline)	Gibco	10010023
YPD (Yeast Peptone Dextrose)	BD Difco	242810
YNB (Yeast Nitrogen Base without amino acid)	BD Difco	291940
CAA (Cas Amino Acid)	BD Difco	223120
LB (Luria Broth)	BD Difco	244620
Critical commercial assays		
DNase I	ThermoFisher Scientific	18047019
Superscript III First-Strand Synthesis System	ThermoFisher Scientific	18080051
DyNAmo Color Flash SYBR Green qPCR Kit	ThermoFisher Scientific	F-416L
BCA-protein assay kit	ThermoFisher Scientific	23227
Human IL-1β ELISA set	BD Biosciences	557953
Human IL-8 ELISA set	BD Biosciences	555244
Human TNF-α ELISA set	BD Biosciences	555212
Mouse IL-1β ELISA set	Invitrogen	88-7013-88
Deposited data		
Raw and processed RNA-Seq data	This study, NCBI's Gene Expression Omnibus (GEO)	GEO accession number: GSE234670 (dataset identifier)
Raw and processed MNase-Seq data	This study, NCBI's Gene Expression Omnibus (GEO)	GEO accession number: GSE234671 (dataset identifier)
Experimental models: Cell lines		
THP-1	ATCC	TIB-202
J774.1	ATCC	TIB-67
Murine peritoneal macrophage cells	The Experimental Animal Facility, Centre For DNA Fingerprinting and Diagnostics	N/A
Experimental models: Organisms/strains		
BALB/c	The Experimental Animal Facility, Centre for DNA Fingerprinting and Diagnostics (CDFD)	N/A
A total of 27 yeast strains	This study	Table S7A
Recombinant DNA		
A total of 9 plasmids	This study	Table S7B
Oligonucleotides		
A total of 108 oligonucleotides	This study	Table S7C
Software and algorithms		
Software: GraphPad Prism8	GraphPad	Graphpad.com
Software: ImageJ	Schindelin et al.[52]	https://imagej.nih.gov/ij/
Software: Adobe Photoshop CS3	Adobe	http://www.adobe.com
Software: Adobe Illustrator CS3	Adobe	http://www.adobe.com
Software: Zen 3.4 Blue	Zeiss	https://www.zeiss.com/microscopy/en/products/software/zeiss-zen.html

Continued

REAGENT or RESOURCE	SOURCE	IDENTIFIER
Software: LAS X	Leica-microsystems	https://www.leica-microsystems.com/products/microscope-software/p/leica-las-x-ls/
Software: IGV	IGV	https://www.igv.org/
Software: BD FACSDIVA v9.0	BD Biosciences	https://www.bdbiosciences.com/en-eu/products/software/instrument-software/bd-facsdiva-software
Other		
Gel Doc Imaging system	Syngene	N/A
ChemicDoc Imaging System	UVITEC Cambridge	N/A
Zen LSM 700microscope	Zeiss	N/A
Zen LSM 900microscope	Zeiss	N/A
Leica confocal microscope	Leica	N/A
BD LSRFortessaTM X-20	BD Biosciences	N/A
Fastprep-24 homogenizer	MP Biomedicals	N/A
Real-Time system Thermo Cycler	Bio-Rad	N/A
Bioruptor	Diagenode	N/A

RESOURCE AVAILABILITY

Lead contact

Further information and requests for resources and reagents should be directed to and will be fulfilled by the lead contact, Rupinder Kaur (rkaur@cdfd.org.in).

Materials availability

This study did not generate new unique reagents

Data and code availability

All data needed to evaluate the conclusions in the paper are present in the paper, or in the supplemental information. The raw RNA-Seq and MNase-Seq data have been deposited to the NCBI's Gene Expression Omnibus (GEO), and are assigned GEO accession numbers of GSE234670 and GSE234671, respectively. Raw data are publicly available as of the date of publication. This paper does not report original code. Any additional information required to reanalyze the data reported in this paper is available from the lead contact upon request.

EXPERIMENTAL MODEL AND STUDY PARTICIPANT DETAILS

Animals

Mice were housed and bred in individually-ventilated cages at a light–dark cycle of 12 h. The ambient temperature was maintained at 22°C, with humidity of 40% $\pm$ 5% at the Experimental Animal Facility of Center for DNA Fingerprinting and Diagnostics (CDFD), Hyderabad, India. Six to eight-week-old female BALB/c mice were used for the experiments performed in this study.

Yeast strains

C. glabrata strains were routinely cultured at 30°C on YPD (1% Yeast extract, 2% Peptone and 2% Dextrose) medium, YNB (0.17% Yeast nitrogen base and 0.05% ammonium sulfate) or CAA (YNB-supplemented with 0.6% casamino acids) medium. *Saccharomyces cerevisiae* and other *Candida* strains were routinely maintained at 30°C on YPD (1% Yeast extract, 2% Peptone and 2% Dextrose) medium. All yeast strains used in this study were grown at 30°C with shaking at 200 rpm, and are listed in Table S7.

Cell lines and primary cells

The human monocytic cell line THP-1 (ATCC #TIB-202) was cultured in RPMI medium supplemented with 10% heat-inactivated FBS, under a humidified atmosphere of 5% CO_2, at 37°C. The murine macrophage cell line J774.1 (ATCC #TIB-67) was cultured in DMEM medium supplemented with 10% heat-inactivated FBS, under a humidified atmosphere of 5% CO_2, at 37°C. All cell lines were *Mycoplasma* contamination

free. Primary murine peritoneal macrophages were cultured in DMEM medium supplemented with 10% heat-inactivated FBS, under a humidified atmosphere of 5% CO_2, at 37°C.

Study approval

Mice infection experiments were conducted at the Experimental Animal Facility of Center for DNA Fingerprinting and Diagnostics (CDFD; www.cdfd.org.in) or the CDFD animal facility, VIMTA Labs Limited (http://www.vimta.com), Hyderabad, India in accordance with guidelines of the Committee for the Purpose of Control and Supervision of Experiments on Animals, Government of India. The protocols were approved by the Institutional Animal Ethics Committees of CDFD (EAF/RK/CDFD/22) and VIMTA Labs Ltd (PCD/CDFD/05). Procedures were designed to minimize animal suffering.

METHOD DETAILS

Strains, plasmids and growth conditions

C. glabrata (*Cg*) *wild-type* (*wt*) and mutant strains, derivatives of the *Cg*-BG2 strain, were maintained on yeast extract-peptone-dextrose (YPD) medium or minimal yeast nitrogen base medium containing Casamino Acid (CAA) at 30°C. The *Escherichia coli* DH5α strain was used for gene cloning and plasmid propagation, and grown in LB medium containing ampicillin at 37°C. To collect logarithmic (log)-phase *Cg* cells, overnight-grown *Cg* strains were re-inoculated at 0.1 OD$_{600}$ in fresh YPD/CAA medium and cultured for 4–5 h at 30°C. *Cg* deletion strains were generated, using the homologous recombination-based approach, wherein the *Cg* gene was replaced with the *nat1* gene, that imparts nourseothricin resistance as a selection marker, as described previously.[53] Double deletion strains were generated by flipping out the *nat1* gene using Flp recombinase, as described previously.[53] Despite multiple attempts, *CgSTH1* could not be deleted, which may reflect essentiality of CgSth1 for *Cg* growth. For generation of double mutants, *Cgsnf2Δepa1Δ* and *Cgyps1-11Δepa1Δ*, *CgSNF2* (*CAGL0M04807g*) and *EPA1* (*CAGL0E06644g*) genes were deleted in *Cgsnf2Δ* and *Cgyps1-11Δ* strain backgrounds, respectively. For complementation analysis, *CgSNF2* (5.193 kb) gene along with 5′ (671 bp)- and 3′ (720 bp)-UTR sequences, was cloned at BamHI and XmaI sites in the pRK1016 (pGRB2.1) vector. For ChIP analysis, *CgSNF2* gene was tagged with the SFB [S-protein(S)-FLAG(F)-Sterptavidin-binding-peptide(B)] epitope at the C-terminus via cloning at SpeI and XmaI restriction sites in the pRK1349 plasmid, which carries *PDC1* promoter. *CgSNF2^{S861D}* was generated by rolling circle method using pRK2404 (*PDC1-CgSNF2-SFB*) plasmid DNA as template. For overexpression analysis, *EPA1* (3.105 kb) gene was cloned in XmaI and XhoI sites, downstream of the strong constitutive *CgPDC1* promoter in the pRK999 vector. The *Candida* strains, plasmids, primers, and antibodies and inhibitors used in this study are listed in Table S7.

Growth analysis

Growth profiles of *Cg* strains in the presence of different stressors were analyzed by serial dilution spot or time course assays in solid and liquid medium, respectively. For spot assay, OD$_{600}$ of overnight-grown *Cg* cultures was normalized to 1.0, and cultures were 10-fold serially diluted in phosphate-buffered saline (PBS), followed by spotting 3 μL of each dilution on appropriate medium, and recording growth after 1 to 2 days of incubation at 30°C. Growth data were either presented as plate-spot images or heatmap. For heatmap generation, a fitness score was assigned to each mutant based on the comparison of mutant's growth with that of the *wt* under the same condition. This score matrix was used to plot heatmap using matrix2png web tool.

For time-course analysis, overnight-YPD medium-grown *Cg* strains were inoculated in fresh YPD medium at an initial OD$_{600}$ of 0.1 and incubated at 30°C with shaking. For growth analysis in YPD and RPMI medium, overnight-YPD medium-grown *Cg* strains were inoculated in either fresh YPD medium or RPMI medium containing 10% FBS (fetal bovine serum) at an initial OD$_{600}$ of 0.1 and incubated at 37°C with 5% CO_2. OD$_{600}$ of cultures was monitored at regular intervals till 36 h, followed by plotting of the absorbance readings as a function of time. Generation time for each strain was calculated during the log-phase (2 h–8 h) of growth.

Cg replication in RPMI medium was determined by colony-forming unit-based assay, wherein overnight-YPD medium-grown *Cg* strains were inoculated in RPMI medium containing 10% FBS (fetal bovine serum) at an initial OD$_{600}$ of 0.1 and incubated at 37°C with 5% CO_2. OD$_{600}$ of cultures was recorded periodically, and appropriate dilution of cultures were plated on YPD medium. After 1–2 days of incubation at 30°C, *Cg* colonies were counted, and CFUs were plotted as a function of time.

Biofilm formation assay

Log-phase, YPD medium-grown *Cg* cells seeded in a 24-well polystyrene plate at an OD$_{600}$ of 0.5. After 90 min incubation at 37°C, non-adherent *Cg* cells were washed off with PBS, and adherent cells were grown in RPMI 1640 medium containing 10% FBS for 48 h at 37°C, with a medium change at 24 h. After removing unbound cells with PBS washes, adherent *Cg* cells were stained with 0.4% (w/v) crystal violet for 45 min, followed by destaining in 95% ethanol. Absorbance of the destaining solution was recorded at 595 nm, *Cg*-lacking blank well absorbance values were subtracted from *Cg*-containing well absorbance values, and biofilm-forming ability of *Cg* mutants was plotted as the biofilm ratio which represents the mutant/*wt* absorbance values. Mutants showing ≥1.25-fold reduction in biofilm ratio were considered to be attenuated for their biofilm-forming capacity.

Mice infection analysis

For animal infection studies, overnight-grown *Cg* strains in YPD medium at 30°C were collected, washed twice with sterile PBS and suspended in PBS to a final cell density of 20 OD$_{600}$. 100 μL of cell suspension was injected into the tail vein of 6–8 week-old female BALB/c mice. At 7th day post-infection, mice were euthanized using CO$_2$ and three organs (kidneys, liver and spleen) were excised out. The harvested organs were homogenized in PBS, and homogenates were appropriately diluted and plated on YPD medium supplemented with penicillin and streptomycin antibiotics. After 1–2 days of incubation at 30°C, *Cg* colonies were counted. The fungal burden in each organ was calculated by multiplying the colony number with the appropriate dilution factor.

Cg-macrophage interaction analysis

Human THP-1 monocytic cells (1 x 10^6 cells in each well of a 24-well tissue culture plate) were treated with phorbol 12-myristate 13-acetate (16 nM) for 12 h for differentiation into macrophages at 37°C with 5% CO$_2$, followed by 12 h cell recovery in RPMI-10% FBS medium. THP-1 macrophages were infected with overnight, YPD medium-grown *Cg* cells at a multiplicity of infection (MoI) of 0.1. Non-phagocytosed *Cg* cells were removed after 2 h, and the infection was continued for another 22 h. At 2 h and 24 h post-infection, extracellular *Cg* cells were removed with PBS, THP-1 cells were lysed in water and lysates were plated on YPD medium. After 2 days of growth at 30°C, *Cg* colonies were counted and the fold replication of *Cg* in THP-1 cells was calculated by dividing 24 h CFU by 2 h CFU counts. % phagocytosis was determined by dividing 2 h CFU by 0 h CFU (Number of *Cg* cells infected to THP-1 macrophages). Mutants showing ≥ 2-fold change in fold replication, as compared to *wt* cells, were considered to have altered survival in macrophages.

Secreted cytokines were measured by enzyme-linked immunosorbent assay (ELISA). For this, THP-1 macrophages were infected with *Cg* at a MoI of 1.0 for 24 h, as described above, and culture supernatants were collected and centrifuged at 1000 rpm to remove any cell debris. IL-1β, IL-8 and TNF-α in cleared supernatants were measured using the ELISA kits following manufacturer's protocol. For inhibitor treatment, PMA-treated THP-1 macrophages were pre-treated with inhibitors or DMSO solvent for 2 h, prior to *Cg* infection, and *Cg*-THP1 co-culture was carried out in the presence of inhibitor or DMSO for 24 h.

For isolation of primary macrophages, 6-8-week-old BALB/c mice were intraperitoneally injected with 1.5 mL of 4% (w/v) thioglycollate. After 5 days, mice were euthanized, and macrophages were collected in DMEM from the mouse peritoneal cavity. Macrophages were centrifuged, suspended in DMEM medium containing 10% heat-inactivated FBS and were seeded in a 24-well plate. *Cg* survival and secreted IL-1β in primary mouse peritoneal macrophages were measured in a similar way, as that for THP-1 cells.

Nucleosome dynamics analysis by MNase-Seq

For MNase-Seq, PMA-activated THP-1 (2.2 x 10^7) cells were infected with overnight YPD medium-grown *wt* cells at a MOI of 1:1, and macrophage-internalized *Cg* cells were collected post 2 h and 10 h infection, after lysing infected macrophages in ice-cold water. Macrophage lysates were gently vortexed to separate *Cg* cells form macrophage debris, followed by centrifugation at 6000 rpm for 5 min at 4°C. The compact *Cg* cell pellet was collected and suspended in ice-cold water, followed by centrifugation at 10,000 rpm for 5 min at 4°C. This step was repeated 3–4 times to obtain *Cg* cell pellet that was devoid of macrophage debris. As a control, overnight YPD medium-grown *wt* cells were grown in RPMI-10% FBS medium for 2 h and 10 h, and cell pellets were collected. After PBS washes, 2 h and 10 h RPMI-grown and macrophage-internalized *wt* cell pellets were suspended in MNase-digestion buffer [10 mM Tris-Cl (pH 8.0) and 1 mM CaCl$_2$], and lysed using glass beads. After lysate centrifugation at 13000 rpm at 4°C for 10 min, lysates (1 mg) were incubated with MNase (10 units/1 mg lysate; NEB #M0247S) at 37°C for 60 min. The MNase digestion was stopped by adding Stop Buffer (8.6% SDS and 0.007 M EDTA), followed by digestion with proteinase K (20 mg/mL) first at room temperature for 30 min, and later at 65°C for overnight. DNA was isolated with PCI (Phenol:Chloroform:Isoamyl alcohol) extraction, precipitated with sodium acetate and ethanol, and was suspended in nuclease-free water, followed by RNase A digestion for 30 min at 37°C. DNA was run on 2% agarose gel, and bands of ∼150 bp, corresponding to mononucleosomal DNA fragments, were excised, purified using QIAquick extraction kit, and were sent to Scigenom, Kochi, India (http://www.scigenom.com/) for library preparation and sequencing. The concentration and quality of purified mononucleosomal DNA was determined by Qubit, Nanodrop and Agilent Tapestation analysis, followed by library generation using the NEBNext Ultra II DNA Library Prep Kit (Illumina), following the manufacturer's instructions. The library quality was assessed using the Agilent Bioanalyzer High Sensitivity DNA chip.

The prepared libraries were sequenced (2x100 bp paired-end sequencing) on the HiSeq 2500 (Illumina) platform, and 40–60 million, high-quality 100 bp reads, with 93% of the total reads passing ≥30 phread score, were generated for each sample. Data were analyzed by DeepSeeq Bioinformatics, Bengaluru, India (https://www.deepseeq.com/). The adapter sequences and low-quality reads were removed using Trimmomatic (version 0.39). Trimmed sequence reads were aligned to the *C. glabrata* genome version s04-m01-r06 (www.candidagenome.org) using bowtie2, version 2.5.0. The percentage alignment varied between RPMI-grown (89–97%) and macrophage-internalized (6–26%) samples. The SAM files generated by bowtie2 were converted to BAM format, sorted and indexed using Samtools, version 1.7. The DANPOS3 software[25] was used to identify the occupancy, position and fuzziness of nucleosomes. For this, clonal reads from BAM files were first removed, followed by quantile normalization. Next, individual dpos, dpeak, and dregion functions from DANPOS3 were used to identify positions, peaks, and regions occupied by nucleosomes in individual samples as well as for compared datasets. Annotation of the called nucleosome position was done using gene start and stop coordinates for 5604 genes, obtained from the C_glabrata_CBS138_version_current_features.gff file version S04-m01-r06 downloaded from http://www.candidagenome.org/download/gff/C_glabrata_CBS138/, by employing the closest function from the Bedtools software version v2.28.0. The –flank_up and –flank_down parameters were set to 500 and 1000, respectively, for TSS (Transcription Start Site) -based analysis, and to 500 and 500, respectively, for TTS (Transcription Termination

Site)-based analysis. Nucleosomes were identified in about 5300 genes in all four-studied conditions. Lastly, three filters, Position shift: ≥50 bp shift, Occupancy change: ≥ 2-fold change (FDR ≤0.05) or Fuzziness change: ≥1.5-fold change (FDR ≤0.05), were applied to identify dynamic nucleosomes.

Immunoblotting analysis

For signaling pathway analysis, PMA-activated macrophages were either left uninfected or infected with *wt* and *Cgsnf2Δ* cells at a MOI of 1:1. After 4 h infection, macrophages were washed with ice-cold PBS, scrapped and centrifuged at 2000 rpm for 5 min. Cell pellets were suspended in freshly-prepared NETN lysis buffer [250 mM NaCl, 5 mM EDTA (pH 8.0), 50 mM Tris-Cl (pH 8.0), and 0.5% Nonidet P-40] containing protease (cOmplete Mini, Roche) and phosphatase (PhosSTOP, Roche) inhibitors, and incubated for 30 min at 4°C. Cell lysates were sonicated for 15 cycles (30 s ON/30 s OFF), with the Diagenode bioruptor sonicator and centrifuged at 13000 rpm for 10 min 120 μg proteins were resolved on 10% SDS-PAGE, and probed with different antibodies. For quantification, intensities of the bands of interest were quantified from independent immunoblots using the ImageJ densitometry software, and normalized with respective GAPDH signal intensities. Values were plotted as a bar graph, considering the signal in control samples as 1.0. For *Cg* protein analysis, log-phase *Cg* cells were lysed using the glass beads, and lysates (80 μg) were resolved on 10% SDS-PAGE, followed by probing with anti-FLAG antibody.

Cg cell wall analysis

For quantification of major cell wall components, overnight YPD medium-grown *wt* and *Cgsnf2Δ* mutant strains were inoculated in fresh YPD medium at 0.1 OD_{600} and incubated at 30°C for 4 h. Log-phase cells (2.0 OD_{600}) were collected, washed and suspended in PBS. Cells were either left untreated or stained with calcofluor white (2.5 μg/mL), fluorescein isothiocyanate-labeled concanavalin A (1 μg/mL) or aniline blue (12.5 μg/mL) for 15 min at room temperature for measurement of chitin, mannan and β-glucan, respectively. After PBS washes, fluorescence intensity of ∼50,000 cells was recorded on BD LSRFortessa X-20 flow cytometer at an excitation/emission wavelength of 405/421, 405/421 and 495/525 nm for β-glucan, chitin and mannan measurement, respectively. Data were acquired and analyzed using the BD FACSDIVA v9.0 software. The background fluorescence was corrected by subtracting the mean intensity fluorescence value of unstained samples from that of respective stained samples. Data were presented as the mean intensity ratio which indicates *Cgsnf2Δ/wt* fluorescence intensity values.

RNA-Sequencing analysis

2 h and 10 h RPMI-medium and macrophage-internalized *wt* and *Cgsnf2Δ* cells were harvested and total RNA was extracted using RNeasy kit (Qiagen), followed by removal of DNA contamination, if any, using DNase I. The purified total RNA was sent to National Genomics Core (NGC) at CDFD, Hyderabad (http://ngc.cdfd.org.in/) for sequencing, which involved mRNA enrichment using Poly(A) mRNA Magnetic Isolation Module, library preparation using NEB Ultra II Directional RNA Library Prep Kit and 150 bp paired-end sequencing on the Illumina NextSeq 2000 platform. Sequenced reads were processed and mapped on the *C. glabrata* CBS138 reference genome using HISAT 2.1.0 aligner.

For gene expression quantification, the counts of mapped reads for each gene were considered using the Feature counts tool, followed by sequencing depth normalization of raw read counts using the DESeq2 tool. Differentially expressed genes were classified based on two criteria: ≥ 2-fold change in expression and adjusted p value of ≤0.05.

Imaging analysis

For morphology analysis, log-phase *Cg* cells were visualized using the LSM700 confocal microscope equipped with 63X/1.44 NA objective. For cell wall chitin staining, log-phase *Cg* cells were stained with calcofluor white (1.25 μg/mL) for 30 min at room temperature. After PBS washes, cells were imaged using LSM700 confocal microscope equipped with 63X/1.44 NA objective. All images were processed using the ZEN blue software.

For immunofluorescence-based Epa1 surface expression analysis, *wt* and *Cgsnf2Δ* cells were grown for 2 h in RPMI medium containing 10% FBS at 37°C with 5% CO₂. Cells were fixed in 3.7% paraformaldehyde for 30 min at 30°C, followed by PBS washes and blocking with 5% BSA for 1 h at room temperature. After overnight incubation with anti-Epa1 antibody at 4°C, cells were washed with PBS and incubated with AlexaFluor 568-conjugated anti-rabbit secondary antibody for 1 h in dark at room temperature. Cells were imaged using the Zeiss LSM900 microscope equipped with plan-apochromate 63X/1.4 NA objective.

For FACS-based Epa1 cell surface expression analysis, fluorescence intensity of anti-Epa1 and Alexa Fluor 488 antibodies-labelled cells (∼50,000) was recorded on BD LSRFortessa X-20 flow cytometer at an excitation wavelength of 491 nm and an emission wavelength of 516 nm. Data were acquired and analyzed using the BD FACSDIVA v9.0 software, and the background fluorescence was corrected by subtracting the mean intensity fluorescence value of unstained samples from that of respective stained samples. Data were presented as the mean intensity ratio which indicates *Cgsnf2Δ/wt* fluorescence intensity values.

For immunofluorescence analysis, J774.1 murine macrophage-like cells (1 x 10⁶) were seeded on a coverslip, and infected with *wt* and *Cgsnf2Δ* cells at a MoI of 1:1. At 2 h post-infection, un-phagocytosed *Cg* cells were removed, followed by 10% FBS-containing DMEM medium addition and incubation for 2 h at 37°C, 5% CO₂. As a control, uninfected J774A.1 cells were grown under similar conditions. J774. 1 cells were washed with ice-cold PBS and fixed with 3.7% (v/v) formaldehyde for 15 min. After fixation, cells were permeabilized with 0.5% (v/v) Triton X-100 in PBS for 5 min, washed twice with PBS and blocked with 10% (v/v) FBS in PBS for 1 h at room temperature. Cells were probed overnight

with anti-NF-κB p65 antibody at 4°C, followed by incubation with AlexaFluor 568-conjugated secondary antibody for 1 h. Coverslips were washed, air-dried and mounted in the VECTASHIELD anti-fade mounting medium containing DAPI. Cells were visualized, and Z-stack images were acquired throughout the nucleus at 1 μm interval using the Leica confocal microscope (63X/1.44 NA objective), and processed using the LAS X software. Each maximum-intensity projection (MIP) image was constructed using 8–12 confocal image subsets. After exporting the MIP image as a TIF file, p65 fluorescence intensity was measured using the ImageJ software, and NF-κB localization was presented as the ratio of fluorescence intensity of nuclear p65 to cytosolic p65.

Quantitative RT-PCR (qRT-PCR) analysis

RNA was isolated from 2 h to 10 h RPMI-grown and macrophage-internalized *Cg* cells using the RNeasy kit (Qiagen), followed by DNase I digestion. 1 μg DNase I-treated total RNA was used for cDNA synthesis using the Superscript III reverse transcriptase, DyNAmo ColorFlash SYBR Green qPCR kit was used to perform qRT-PCR, and gene expression was determined by the $2^{-\Delta\Delta CT}$ method. *GAPDH/ACT1* expression was used as an internal reference control to normalize the gene expression data.

Chromatin immunoprecipitation (ChIP) analysis

ChIP was performed, as described previously.[54] Briefly, *CgSNF2-SFB*-expressing *Cgsnf2Δ* was grown in CAA medium for 4 h, followed by formaldehyde crosslinking. Next, cells were lysed in buffer containing 1 mM EDTA [pH 8.0], 50 mM HEPES [pH 7.5], 0.1% sodium deoxycholate [w/v], 140 mM NaCl, 1× protease inhibitor cocktail, and 1% Triton X-100 by bead-beating, and sonicated for 40 min [30 s pulses of on and off] to obtain 250-500 bp small chromatin fragments. A fraction of the clear supernatant was used as Input fraction, while the remainder was subjected to immunoprecipitation with anti-IgG or anti-FLAG antibody. After de-crosslinking, DNA was purified using phenol:chloroform:isoamyl alcohol. Both purified ChIPed and input DNA samples were used as template for qRT-PCR. Fold enrichment in ChIPed samples was calculated using the $2^{-\Delta\Delta Ct}$ method, and results are presented as enrichment over IgG.

Nucleosome density analysis

wt and *Cgsnf2Δ* strains were grown in RPMI medium for 2 h at 37°C. Cells were collected, washed with ice-cold PBS, suspended in MNase-digestion buffer [10 mM Tris-Cl (pH 8.0) and 1 mM CaCl$_2$] and were lysed using glass beads. After centrifugation at 13000 rpm at 4°C for 10 min, lysates (1 mg) were incubated with MNase (10 units/1 mg lysate; NEB #M0247S) at 37°C for 60 min 10% of whole cell lysates was kept as undigested control. After stopping MNase digestion with Stop Buffer (8.6% SDS and 0.007 M EDTA), DNA was isolated from undigested (control) and MNase-digested samples using Phenol:Chloroform:Isoamyl alcohol extraction method. DNA was precipitated with sodium acetate and ethanol, and was suspended in the nuclease-free water, followed by RNase A digestion for 30 min at 37°C. MNase-digested DNA was run on 2% agarose gel, and bands of ~150 bp, corresponding to the mononucleosomal DNA fragments, were excised and purified using QIAquick extraction kit. MNase-digested and undigested (control) DNA samples were used as template for quantitative-PCR using four sets of primers covering 520 bp region of the *EPA1* promoter. The nucleosome occupancy on *EPA1* promoter was calculated by dividing the Ct values of MNase-digested sample by those of undigested samples, and presented as fold enrichment.

Functional enrichment analysis

The DAVID tool (https://david.ncifcrf.gov/) with default settings was used for enrichment of gene ontology (GO) terms for biological process, cellular component and molecular function, in genes with dynamic nucleosomes at their promoters and in differentially-expressed genes. Terms with the p value of ≤0.05 were considered as enriched in gene datasets.

QUANTIFICATION AND STATISTICAL ANALYSIS

Statistical significance was determined using the two-tailed Student's t test, or the nonparametric Mann-Whitney test in the GraphPad Prism software. The multiple amino acid sequence alignment was done using the Clustal W tool. Error bars indicate standard error of the mean (s.e.m). The n represents the number of biological replicates for each experiment, and is provided in Figure Legends, along the statistical analysis details. Asterisks were used to represent p values: *p ≤ 0.05; **p ≤ 0.01; ***p ≤ 0.005; ****p ≤ 0.001. The p value of ≤0.05 was considered significant.